Proteome dynamics reveal Leiomodin 1 as a key regulator of myogenic differentiation

Ellen Späth[1*], Svenja C. Schüler[1,2*], Ivonne Heinze[1], Therese Dau[1], Alberto Minetti[1], Maleen Hofmann[1], Julia von Maltzahn[1,3#] and Alessandro Ori[1#]

Affiliations

1 - Leibniz Institute on Aging - Fritz Lipmann Institute (FLI), Jena, Germany

2 - Département de Pharmacologie - Physiologie, Université de Sherbrooke, QC, Canada

3 - Brandenburg Technische Universität Cottbus-Senftenberg, Universitätsplatz 1, 01968 Senftenberg, Germany, Faculty of Health Sciences and Faculty for environment and natural sciences

[*] Contributed equally

[#] Correspondence should be addressed to: alessandro.ori@leibniz-fli.de or julia.vonmaltzahn@b-tu.de

Abstract

During myogenic differentiation the cellular architecture and proteome of muscle stem cells and myoblasts undergo extensive remodeling. These molecular processes are only partially understood and display alterations in disease conditions as well as during aging resulting in impaired regeneration. Here, we used mass spectrometry to quantify the temporal dynamics of more than 6000 proteins during myogenic differentiation. We identified the actin nucleator leiomodin 1 (LMOD1) among a restricted subset of cytoskeletal proteins increasing in abundance in early phases of myogenic differentiation. We show that LMOD1 is already expressed by muscle stem cells *in vivo* and displays increased abundance during skeletal muscle regeneration, especially during early regeneration suggesting that LMOD1 is important for induction of myotube formation. Of note, knockdown of LMOD1 in primary myoblasts and during skeletal muscle regeneration severely affects myogenic differentiation, while overexpression accelerates and improves the formation of myotubes suggesting that LMOD1 is a critical component regulating myogenic differentiation. Mechanistically, we show that LMOD1 physically and functionally interacts with the deacetylase sirtuin1 (SIRT1), a regulator of myogenic differentiation, especially at the onset of myogenic differentiation. We demonstrate that LMOD1 influences SIRT1 localization and the expression of a subset of its target genes. Consistently, depletion or pharmacological inhibition of SIRT1 partially rescues the impairment of myogenic differentiation observed after knockdown of LMOD1. Our work identifies a new regulator of myogenic differentiation that might be targeted to improve muscle regeneration in aging and disease.

Keywords: muscle stem cell, satellite cell, cytoskeleton, myogenesis, LMOD1, SIRT1, mass spectrometry, myogenic differentiation, regeneration

36 **Main Text**

37 Muscle stem cells (MuSCs), also known as satellite cells, possess a remarkable ability to
38 regenerate adult skeletal muscle following injury (Sambasivan et al. 2011; Murphy et al. 2011).
39 These cells are typically quiescent, reside between the basal lamina and the myofiber (Mauro
40 1961; Sousa-Victor et al. 2015), and are characterized by the expression of the paired box
41 transcription factor 7 (PAX7) (Seale 2003; Lepper, Partridge, and Fan 2011; von Maltzahn et
42 al. 2013; Zammit et al. 2006). In response to physiological and regeneration-inducing stimuli,
43 MuSCs become activated, begin to self-renew, and undergo myogenic differentiation (Fu,
44 Wang, and Hu 2015; Schmidt et al. 2019). During myogenic differentiation after injury - a
45 process recapitulating myogenesis during development - MuSCs proliferate, differentiate, and
46 finally fuse to damaged myofibers or form new myofibers. These processes are tightly
47 regulated by the expression of different myogenic regulatory factors (MRFs) such as MYF5,
48 MYOD, myogenin and MRF4 (Chang and Rudnicki 2014; Schmidt et al. 2019; Tiffin et al.
49 2003). Additionally, external cues from the surrounding microenvironment play a crucial role
50 in regulating myogenic differentiation (Bentzinger, Wang, Dumont, et al. 2013; Hung et al.
51 2023). These cues involve different signaling pathways including NOTCH, WNT, BMPs, FGFs,
52 and Hedgehog (Fre et al. 2005; Baghdadi, Castel, et al. 2018; Baghdadi, Firmino, et al. 2018;
53 Bentzinger, Wang, von Maltzahn, et al. 2013; Friedrichs et al. 2011; Larraín et al. 1997;
54 Voronova et al. 2013). Epigenetic mechanisms and chromatin remodeling regulate the
55 accessibility of transcription factors to regulatory regions of the DNA and, thereby, the
56 expression of myogenic genes (Saccone and Puri 2010; Massenet et al. 2021). Histone
57 deacetylases (HDACs) and methyltransferases, e.g., SIRT1 (Ryall et al. 2015), HDAC4
58 (Moresi et al. 2012; Finke et al. 2022) and SMYD3 (Codato et al. 2019) are implicated in
59 maintaining muscle integrity and differentiation. The cytoskeleton plays crucial roles in
60 regulating cell shape, motility and signal transduction (Pollard and Cooper 2009; Higuchi-
61 Sanabria et al. 2018). This is especially important during fusion of myoblasts to form myotubes
62 (Abmayr and Pavlath 2012). Perturbations in signalling pathways, mechanosensitivity, and
63 interactions with the extracellular matrix (ECM) were shown to significantly affect the
64 cytoskeletal architecture of MuSCs in disease and during aging (Chakkalakal et al. 2012;
65 Hwang and Brack 2018; Lukjanenko et al. 2016). For instance, in Duchenne muscular
66 dystrophy (DMD), mutations in the dystrophin gene can disrupt the connection between the
67 actin cytoskeleton and the ECM, impairing the function of MuSCs (Winder, Gibson, and
68 Kendrick-Jones 1995; Lu-Nguyen et al. 2017; Mournetas et al. 2021). Similarly, mutations in
69 plectin, a protein that connects various cytoskeletal components, result in muscle diseases
70 known as plectinopathies, which are characterized by compromised muscle cell integrity
71 (Winter and Wiche 2013). Of note, also age-related sarcopenia can be caused by changes in
72 cytoskeletal proteins, resulting in a decline in myofiber quantity and functionality (Budai,

73 Balogh, and Sarang 2018; Larsson et al. 2019). Changes in actin dynamics, e.g., a
74 dysregulation of ARP2/3 and N-WASP, responsible for forming branched actin networks and
75 cell motility, can impair the response to muscle injury (Lai and Wong 2020). Additionally, the
76 distribution of desmin, an essential protein for structural integrity, was shown to affect the
77 mechanical properties and resilience of myofibers (Meyer, Schenk, and Lieber 2013). Aging
78 also affects muscle regulatory factors like MyoD and myogenin, disrupting the timely
79 expression of cytoskeletal and contractile proteins required for proper differentiation of MuSCs
80 (Sousa-Victor et al. 2014).
81 Here, we set out to identify new regulators of myogenic differentiation by investigating
82 alterations in protein dynamics during myogenic differentiation using mass spectrometry.
83 Thereby, we identified LMOD1 among a restricted group of cytoskeletal proteins that increases
84 in abundance during early myogenic differentiation. We confirmed the presence of LMOD1 in
85 MuSCs *in vivo* and show that LMOD1 is transiently upregulated during skeletal muscle
86 regeneration and that reducing LMOD1 expression after injury impairs skeletal muscle
87 regeneration. LMODs are known as powerful actin filament nucleator but their role in myogenic
88 differentiation has not been investigated so far (Chereau et al. 2008; Boczkowska et al. 2015;
89 Fowler and Dominguez 2017; Tolkatchev, Gregorio, and Kostyukova 2022). Through
90 knockdown and overexpression experiments, we show that LMOD1, but not the closely related
91 LMOD2, is essential for proper myogenic differentiation. Mechanistically, we show that
92 LMOD1 interacts with the deacetylase SIRT1, a known regulator of myogenic differentiation
93 (Fulco et al. 2003; Ryall et al. 2015), and thereby influence its subcellular localization and the
94 expression of a subset of target genes.

95 **Proteome dynamics during myogenic differentiation**

96 To comprehensively and unbiasedly examine the protein dynamics during myogenic
97 differentiation, we performed an *in vitro* five-day differentiation time course experiment using
98 mouse primary myoblasts from five different mice (Figure 1A) and collected samples at each
99 day of differentiation for label-free quantitative proteomics (Table S1). Principal Component
100 Analysis (PCA) based on protein intensities obtained from mass spectrometry data (6098
101 quantified proteins in total) revealed a progressive separation of the different cell populations
102 by the day of differentiation (Figure 1B). We confirmed the expected dynamics of key
103 myogenic regulators by qRT-PCR and mass spectrometry (Schmidt et al. 2019), validating our
104 experimental setup and proper myogenic differentiation (Figures 1C and 1D). Next, we
105 compared protein dynamics by clustering the obtained proteomics data (Table S1). The 3839
106 protein groups significantly affected in at least one measured time point of differentiation
107 relative to undifferentiated myoblasts were assigned to six clusters by k-means clustering
108 (Figure 1E). Each cluster displayed distinct dynamics and was enriched for specific KEGG
109 pathways (Figure 1F). Notably, cluster 2 included proteins that progressively increased in
110 abundance during differentiation and were closely associated with muscle contraction and
111 function as well as cytoskeletal dynamics e.g. Actinin Alpha 2 (ACTN2), Tropomyosin alpha-
112 1 and -3 (TPM1, TPM3) Leiomodin 1 (LMOD1) and Dystrophin (DMD) (Figure 1G). These
113 findings confirm the importance of cytoskeletal dynamics during myogenic differentiation but
114 also raise questions about the molecular mechanism responsible for this shift in the proteomic
115 landscape.

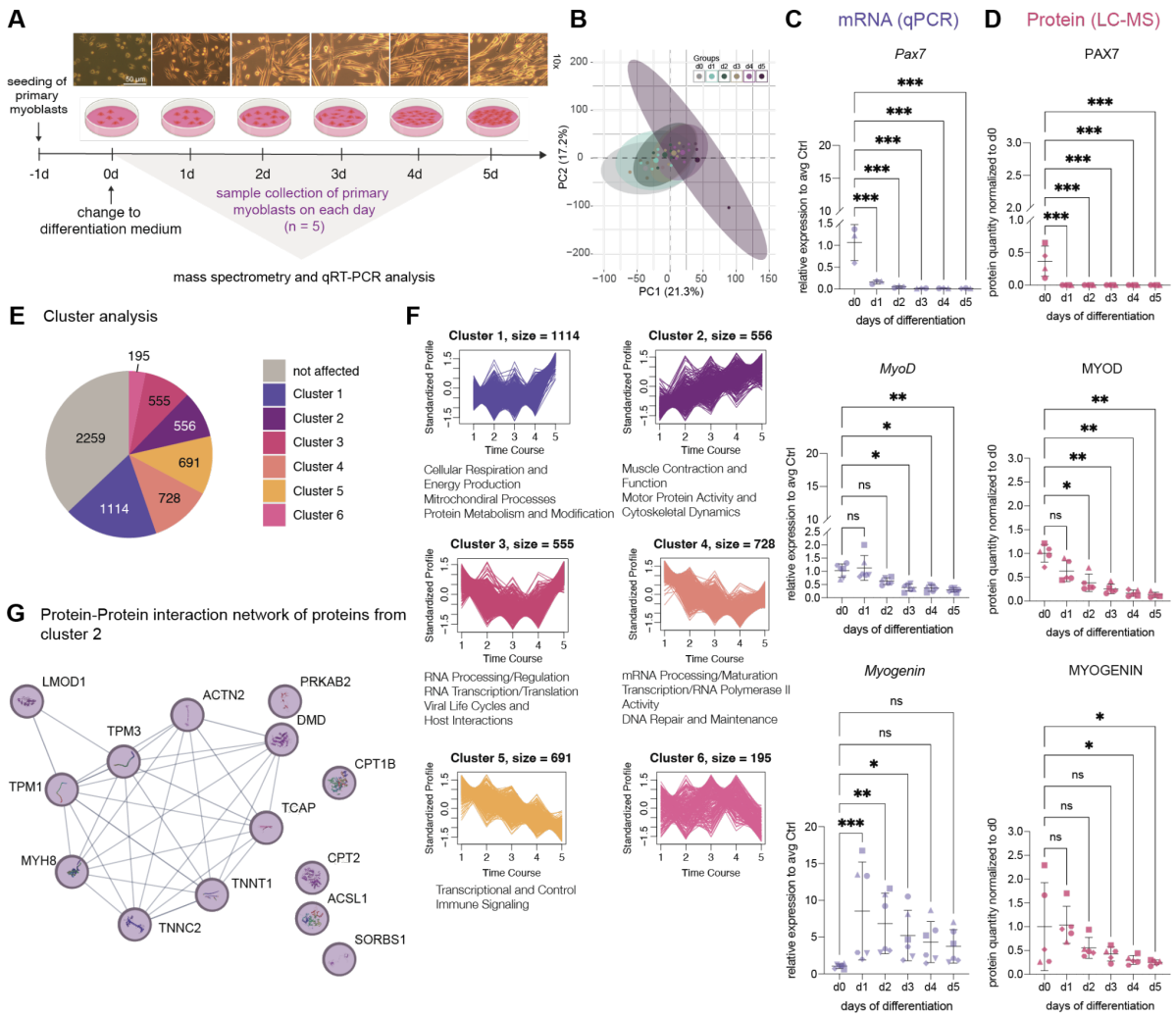

Figure 1: Analysis of the proteome shows dynamic alterations during myogenic differentiation
A. Experimental workflow for analyzing the five-day differentiation time course using mass spectrometry (Table S1) and qRT-PCR. Primary myoblasts isolated from five individual mice were seeded and differentiated for up to five days. **B**. Principal component analysis (PCA) of proteomics data. Ellipses represent a 95 % confidence interval for each day of differentiation. **C**. qRT-PCR analysis showing the relative mRNA expression of *Pax7*, *MyoD*, and *Myogenin*, normalized to *Gapdh* and day 0. **D**. Mass spectrometry-based quantification of PAX7, MYOD and MYOGENIN protein levels normalized to day 0. **E**. Pie chart for proteome dynamics. 6098 protein groups were subjected to k-means clustering analysis, 2259 were unaffected, while 3839 protein groups showed significant changes (Absolute AVG log2 ratio>0.58 and Q value<0.25) in expression levels in at least one-time point compared to day 0. Protein groups were classified into six clusters based on their expression dynamics using k-means clustering. **F.** Clusters showing distinct protein abundance dynamics during myogenic differentiation and KEGG pathways enriched (FDR <0.05) in each cluster (Table S1). **G.** Proteins from cluster 2 were chosen according to KEGG pathway annotation: striated muscle contraction and function, motor protein activity and cytoskeletal dynamics. The protein-protein interaction network was visualized with STRING (Szklarczyk et al. 2011), edge confidence: medium 0.4. For (**C**) and (**D**): In all bar plots, each symbol represents a biological replicate, and the error bars indicate the standard deviation. (SD). One-way, ANOVA. *: q value ≤ 0.05, **: q value ≤ 0.01, ***: q value ≤ 0.001.

134 **LMOD1 levels increase during early myogenic differentiation, in aged MuSCs and**
135 **regenerating skeletal muscle**
136 Given the role of cytoskeleton remodeling as one of the drivers of myogenic differentiation, we
137 focused on this cluster of proteins and specifically looked for proteins that increased early
138 during the differentiation process. Among these, we found two proteins encoded by paralog
139 genes, namely leiomodin 1 (LMOD1) and leiomodin 2 (LMOD2) (Figure 2A), which share
140 67.05 % sequence similarity, although varying in their number of amino acids and expression
141 across tissues (Qualmann and Kessels 2009; Fowler and Dominguez 2017). Interestingly, the
142 expression pattern of LMOD1 and LMDO2 during myogenic differentiation displayed
143 differences: while LMOD1 showed a significant increase at the beginning (day 1) of myogenic
144 differentiation, LMOD2 increased later in the process (Figure 2A) suggesting that LMOD1
145 might be a key protein in driving early myogenic differentiation. To assess the *in vivo* relevance
146 of our finding, we queried two proteomic datasets of freshly isolated MuSCs and four different
147 skeletal muscles (gastrocnemius, G; soleus, S; tibialis anterior, TA; extensor digitorum longus,
148 EDL) (Schüler et al. 2021). We found LMOD2 to be the most abundant leiomodin in whole
149 skeletal muscle, as expected (Yuen et al. 2022; Tsukada et al. 2010), while the overall
150 abundance of LMOD1 was lower since this protein has been mainly associated with smooth
151 muscle cells (Nanda and Miano 2012; Conley et al. 2001; Nanda et al. 2018) (Figure 2B).
152 Surprisingly, we detected LMOD1, but not LMOD2, in freshly isolated MuSCs, and noted that
153 the protein levels of LMOD1 increased in MuSCs isolated from old mice (Figure 2C and Figure
154 S1B). To independently validate this finding, we performed immunofluorescence stainings on
155 cryosections of TA muscles from young and geriatric mice. Consistent with previous
156 publications, we observed a reduction in the number of PAX7+ cells with increasing age
157 (Brack, Bildsoe, and Hughes 2005; Shefer et al. 2006; Yamakawa et al. 2020) (Figure S1C).
158 Furthermore, we confirmed the age-related increase of LMOD1 abundance in MuSCs (Figure
159 2D and Figure S1B). Of note, this was accompanied by a significant increase in the number
160 of LMOD1+/PAX7+ cells in sections of geriatric compared to young mice (Figure 2E).
161 Interestingly, we found LMOD1 to be mainly located in the cytoplasm of PAX7+ cells in TA
162 muscles from young mice (Figure 2D and S1D). However, in TA muscles from geriatric mice,
163 we found a significantly higher number of PAX7+ cells that displayed nuclear localization of
164 LMOD1 (Figure 2F), suggesting that LMOD1 accumulates and mis-localizes in MuSCs with
165 increasing age and could be one contributing factor to the reduced ability of MuSCs in aged
166 mice to differentiate.
167 Finally, we investigated the expression of LMOD1 during regeneration of skeletal muscle *in*
168 *vivo.* Therefore, we performed a regeneration time course experiment following cardiotoxin
169 (CTX) injury and assessed LMOD1 expression by immunoblot and immunofluorescence
170 analyses in young mice (Figure 2G and Figure 2H). We observed low abundance of LMOD1

171 in uninjured TA muscle but found a progressive increase in abundance up to day 7 after injury
172 and a decrease thereafter (Figure 2G). Immunofluorescence staining confirmed that LMOD1
173 was highly abundant in myofibers at day 5 after injury when mostly newly formed regenerating
174 myofibers are present, hinting at a functional role of LMOD1 in early myogenic differentiation.
175 Of note, LMOD1 abundance was barely detectable at day 7 and later time points suggesting
176 that LMOD1 abundance decreases during maturation of myofibers (Figure 2H). In conclusion,
177 these findings demonstrate that LMOD1 abundance is not only increased at the onset of
178 myogenic differentiation *in vitro* but is also expressed by MuSCs under homeostatic conditions
179 *in vivo* and in MuSC and newly formed myofibers following injury, indicating its importance for
180 myofiber differentiation and skeletal muscle regeneration.

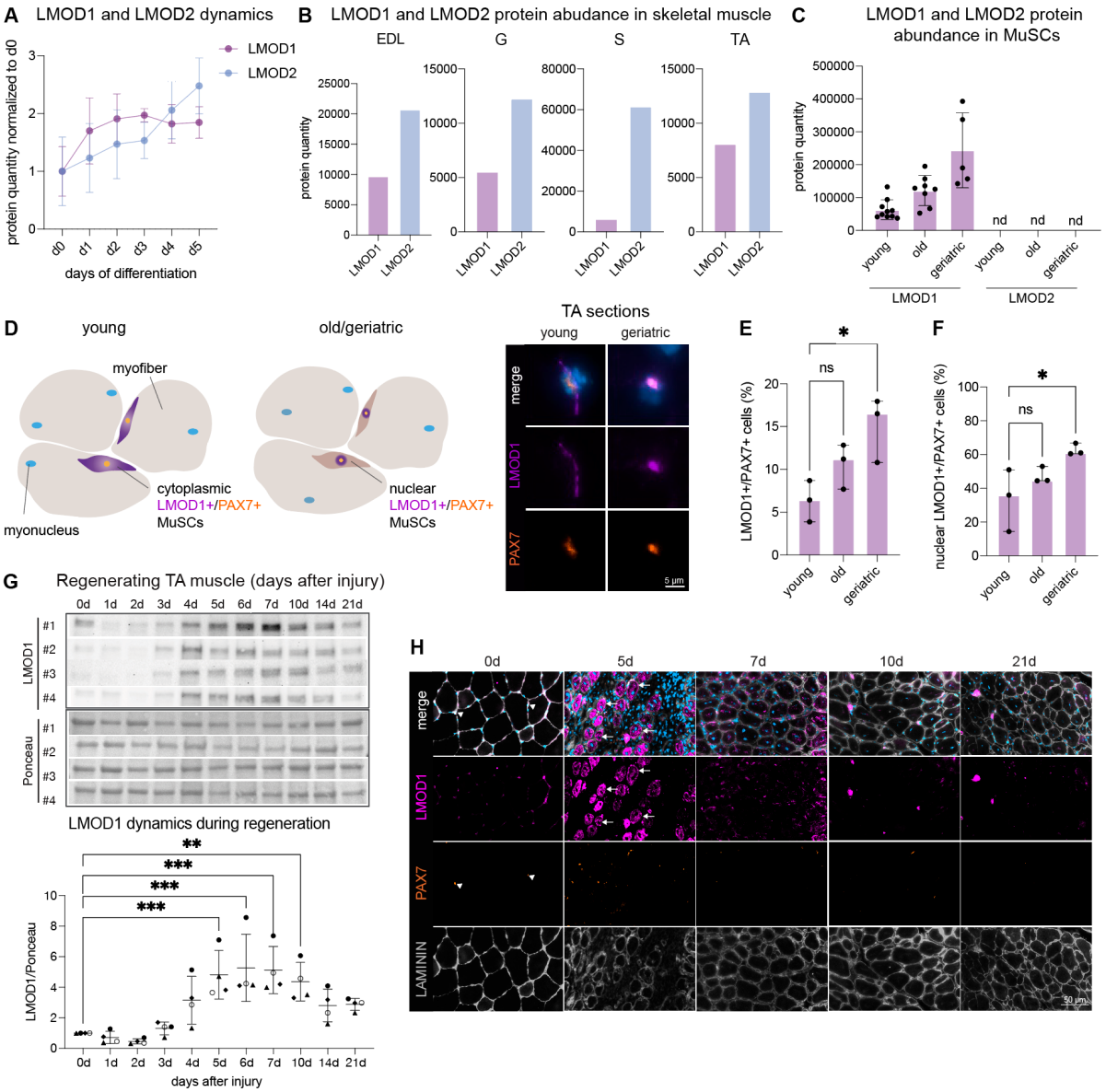

181

182 **Figure 2: LMOD1 increases during early myogenic differentiation and is upregulated in aged MuSCs**
183 **A**. Protein quantification of LMOD1 and LMOD2 during myogenic differentiation, based on mass spectrometry data
184 and normalized to the protein amount of day 0. Error bars indicate SD, and colored dots indicate the mean value
185 of the biological replicates (n = 5). **B.** LMOD1 and LMOD2 protein abundance estimated from mass spectrometry

data in different skeletal muscles (gastrocnemius, G; soleus, S; tibialis anterior, TA; extensor digitorum longus, EDL). Displayed values are averages of n = 5 samples from individual mice. Mass spectrometry data from (Schüler et al. 2021). **C**. LMOD1 and LMOD2 protein quantity in MuSCs obtained from young (n = 10), old (n = 8) and geriatric (n = 5) mice, nd = not detected. Mass spectrometry data from (Schüler et al. 2021). **D**. Representative immunofluorescence images of LMOD1 (purple), PAX7 (orange), and Hoechst (blue) of TA sections from n = 3 individual mice per age group: young (3-month-old) and old (18-months-old), geriatric (33-months-old) mice. Scale bar: 5 µm. **E.** Ratio of PAX7+ and LMOD1+ cells normalized to the cells positive for PAX7+ (Figure S2C) and **F.** Quantification of the percentage of PAX7+ cells showing nuclear LMOD1 localization. Related to Figure S1. For (**E**) and (**F**): One-way, ANOVA. *: q value ≤ 0.05, **: q value ≤ 0.01, ***: q value ≤ 0.001. In all bar plots, each black dot represents a biological replicate, and the error bars indicate the SD. **G**. Muscle regeneration time course: Immunoblot of LMOD1 levels in regenerating TA muscle after injury. Quantification of LMOD1 levels normalized to Ponceau and relative to the LMOD1 signal at day 0. Each symbol represents a biological replicate, and error bars represent SD. One-way ANOVA; **: p-value ≤ 0.01, ***: p-value ≤ 0.001. **H.** Representative immunofluorescence images of LMOD1 (purple), PAX7 (orange), LAMININ (grey), and Hoechst (blue) of TA sections at different days post-injury from young mice (3 months old). The white arrowhead shows PAX7+ cells at day 0, white arrows indicate newly formed LMOD1+ myofibers at day 5. Scale bar: 50 µm.

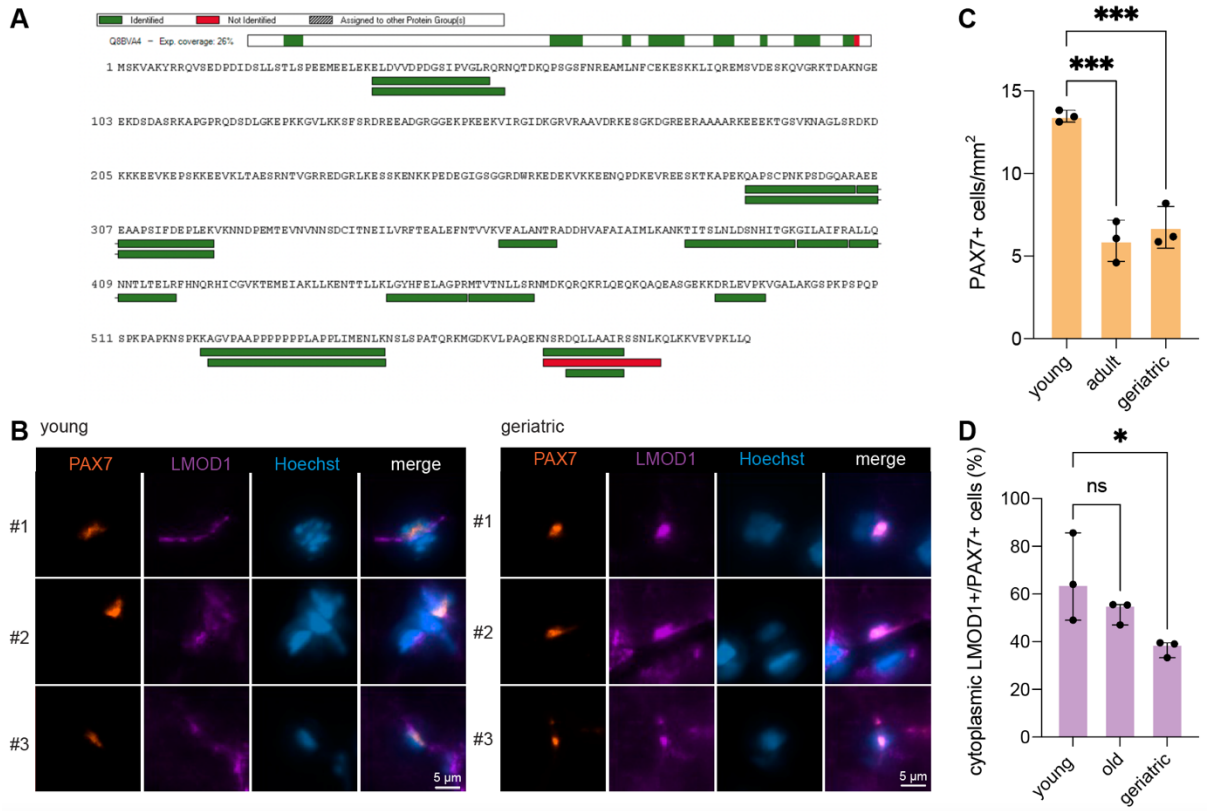

Figure S1: LMOD1 in MuSCs and skeletal muscle

A. LMOD1 protein coverage in proteomics data from MuSCs. Multiple unique (proteotypic) peptides were identified. Data from (Schüler et al. 2021). **B**. Immunofluorescence images of TA sections from different mice (n = 3) per age group of young (3 months old) and geriatric (33 months old) mice. PAX7 (orange), LMOD1 (purple) and Hoechst (blue). **C**. Number of PAX7+ cells per mm^2 cells in muscle sections from young, old and geriatric mice and **D**. Quantification of PAX7+ cells showing cytoplasmic LMOD1 localization. For (**C**) and (**D**): One-way ANOVA; *: p-value ≤ 0.05, ***: p-value ≤ 0.001, ns: not significant. In all bar plots, each black dot represents a biological replicate, and the error bars indicate the SD. Related to Figure 2.

212 **Knockdown of *Lmod1* impairs myogenic differentiation, while overexpression of**
213 ***Lmod1* accelerates myotube formation**
214 The early increase of abundance of LMOD1 during myogenic differentiation suggests a
215 potential functional role for this protein in promoting the initiation of myogenic differentiation.
216 To test this hypothesis, we used a small interfering RNA (siRNA) to reduce LMOD1 expression
217 and analyzed the impact on myoblast proliferation (Figure S2A) and differentiation (Figure 3A).
218 We confirmed the successful knockdown of *Lmod1* mRNA by qRT-PCR (Figure S2B and S2F)
219 and reduced levels of LMOD1 protein by immunoblot analysis (Figure S2C and S2G). After 48
220 hours of proliferation, we observed a slight (26 %) but significant decrease in the number of
221 proliferating Ki67-positive myoblasts upon knockdown of LMOD1 (Figure S2D and S2E).
222 During myogenic differentiation, the cell population becomes heterogeneous with a distinct
223 expression of myogenic markers (such as MyoD, myogenin, and devMHC) determining
224 cellular identity thereby controlling the potential to differentiate and ultimately form new
225 myofibers (Figure 3B). We characterized the cell populations after knockdown of LMOD1
226 based on the expression of myogenic markers using immunofluorescence staining at day
227 three of differentiation (Figure 3C and S2M-Q). We found that the reduced levels of LMOD1
228 resulted in an increased frequency of cells with a pronounced spherical phenotype, also
229 identified as non-elongated, MHC-positive cells (Figure 3C and 3E). Moreover, a significant
230 reduction in the number of nuclei per myotube was observed upon knockdown of LMOD1,
231 indicating a potential role in the fusion process (Figure 3D). Furthermore, we observed
232 significantly shorter myotubes upon knockdown of LMOD1, supporting our previous finding
233 that the cells are unable to properly differentiate (Figure 3F).
234 Given the structural similarities between LMOD1 and LMOD2, we set out to determine if
235 individual knockdown in primary myoblasts induces similar phenotypes during myogenic
236 differentiation (Figure 3G). Knockdown of both *Lmod1* and *Lmod2* mRNA was validated by
237 qRT-PCR (Figure S2I) and confirmed at the protein level by immunoblot (Figure S2J).
238 Interestingly, the knockdown of LMOD2 did not lead to any noticeable phenotypes compared
239 to primary myoblasts transfected with a scramble control siRNA (Figure 3H and S2K).
240 However, we observed a significant reduction in the number of nuclei per myotube (Figure 3I),
241 increased frequency of non-elongated MHC-positive cells (Figure 3J), and increased number
242 of shorter myotubes (Figure 3K) in the *Lmod1/2* double knockdown. These data suggest that
243 LMOD1 is required for myogenic differentiation in primary myoblasts, while LMOD2 appears
244 to be dispensable.
245 To examine how reduced levels of LMOD1 affect skeletal muscle regeneration *in vivo*, we
246 injured the TA-muscle of 3-months-old mice using CTX, followed by injection of a self-
247 delivering siRNA targeting Lmod1 (Figure 3L) at day 3 after injury, a time point when MuSCs
248 start to differentiate. Subsequently, TA-muscles were isolated at day 5 after injury, the time

249 when LMOD1 was previously shown to be highly expressed in newly formed myofibers.
250 Knockdown of *Lmod1* led to a significant reduction in the number of cells expressing the early
251 differentiation marker myogenin (Figure 3M and 3N), suggesting a critical role for LMOD1 in
252 the transition of MuSCs from proliferation to differentiation. Together, these findings indicate
253 that LMOD1 is not only important for myofiber formation but may also play a key regulatory
254 role in the differentiation of MuSCs into myoblasts and myocytes during the muscle
255 regeneration process stressing its role in controlling myogenic differentiation.
256 To test whether LMOD1 alone is sufficient to promote myogenic differentiation, we generated
257 six independent primary myoblast cultures that were stably transduced with a virus to
258 overexpress either LMOD1 or GFP (Figure 3O). Overexpression (OE) of Lmod1 mRNA by
259 qRT-PCR (Figure S2L) and protein by immunoblot (Figure S2M) was confirmed by comparison
260 to a GFP OE control. Immunofluorescence analysis (Figure 3P and S2O) after one day of
261 differentiation showed that overexpression of LMOD1 promotes myogenic differentiation, as
262 shown by a higher number of nuclei per myotube (Figure 3Q). Additionally, we observed an
263 accelerated formation of fully differentiated myotubes (Figure 3Q) and an increase in myotube
264 length (Figure S2N) in LMOD1 OE cells compared to the GFP OE control construct. To further
265 characterize the molecular alterations induced by overexpression of LMOD1 during myogenic
266 differentiation, we generated proteomics data from LMOD1 overexpressing and GFP control
267 cells at multiple time points of differentiation (Table S2). Using gene set enrichment analysis,
268 we found that at day 1 of differentiation, cells overexpressing LMOD1 exhibit higher levels of
269 proteins that are up-regulated at the beginning of differentiation, such as HSPB3, ALDH3A1,
270 SMTNL2, ACTG1, when compared to the GFP control group (Figure S2P) (Table S2). This
271 proteome signature corroborates the observation that LMOD1 overexpression is sufficient to
272 promote myogenic differentiation.

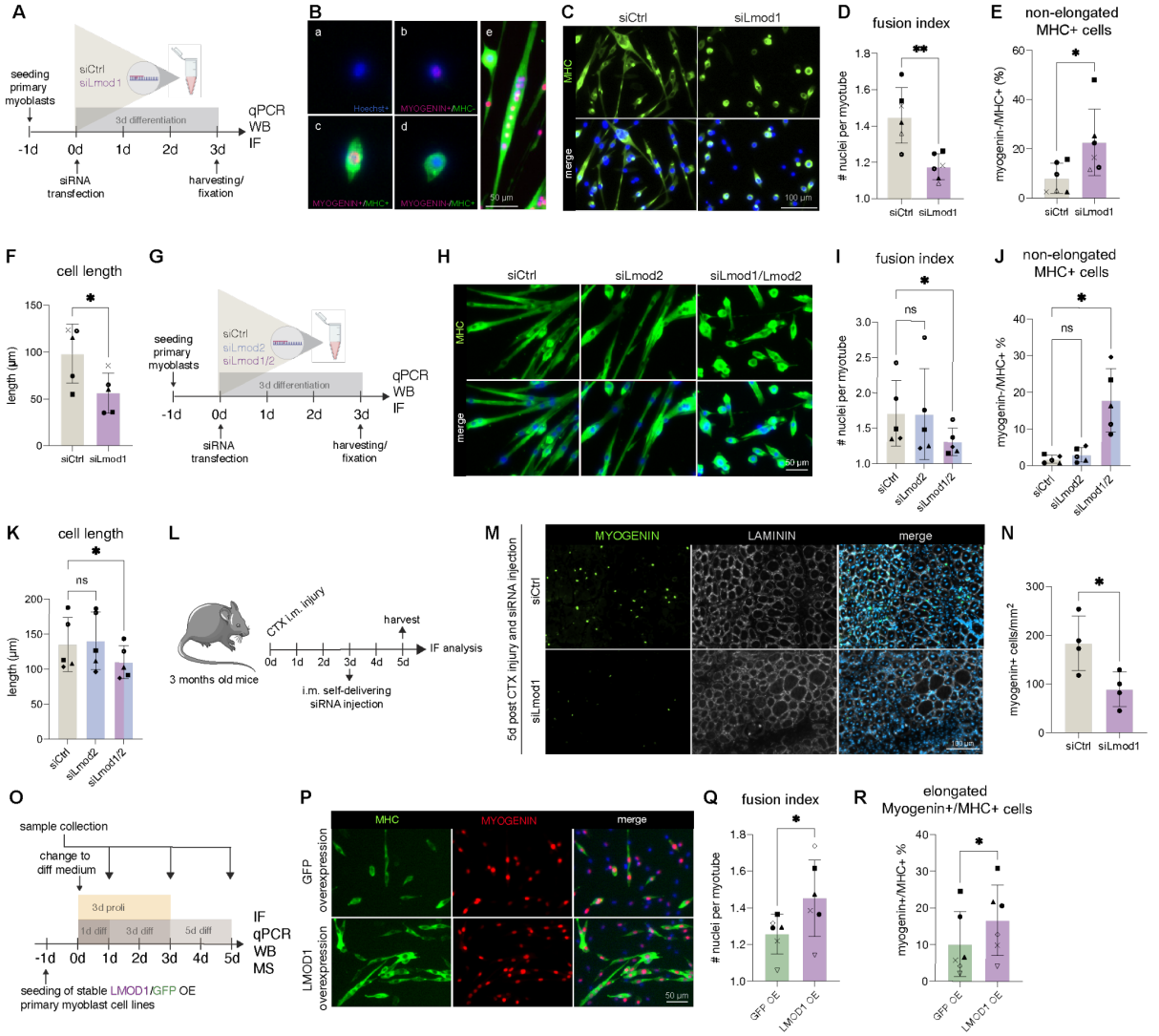

Figure 3: Knockdown of *Lmod1* impairs myogenic differentiation and reduces muscle regeneration, while overexpression enhances it.

A. Schematic of the *Lmod1* knockdown experiment after 3 days of differentiation. siRNA directed against *Lmod1* or scramble (siCtrl) control was used to transfect primary myoblasts isolated from individual mice. Differentiation was induced by a change to differentiation medium at 0h. **B.** Overview of quantified different cell types based on their expression of myogenic markers; Myogenin (red), Myosin heavy chain (MHC) (green), Hoechst (blue). Scale bar: 50 µm. (a) reserve cells: Hoechst+/Myogenin-/MHC- and undifferentiated. (b) Myogenin+/MHC-: Myogenin positive, MHC negative, just started to differentiate. (c) Myogenin+/MHC+: co-express bot in the process of differentiation. (d) Myogenin-/MHC+: non elongated. (e) Fully differentiated myotubes: quantified by nuclei count to assess the fusion process. **C.** Representative immunofluorescence images after three days of differentiation and siCtrl or siLmod1 transfection; MHC (green), nuclei (blue). Scale bar: 100 µm. **D - F.** Quantification of the number of nuclei per myotube (**D**), Myogenin-/MHC+ cells (**E**) and length of differentiated myotubes (in µm) (**F**). Paired t-test; *: p-value ≤ 0.05, **: p-value ≤ 0.01. **G.** Schematic of the *Lmod2* and *Lmod1/Lmod2* double knockdown experiment after 3 days of differentiation. siRNA against *Lmod1*, *Lmod2*, both or scramble (siCtrl) was used to transfect primary myoblasts. Differentiation was induced by a change to differentiation medium at 0h. **H.** Representative immunofluorescence images of siLmod2 and siLmod1/Lmod2 double knockdown after three days of differentiation; devMHC (green), nuclei (blue). Scale bar: 50 µm. **I - K.** Quantification of the number of nuclei per myotube (**I**), Myogenin-/MHC+ cells (**J**), Length of differentiated myotubes (in µm) (**K**). One-way ANOVA; *: p-value ≤ 0.05, ns: not significant. **L**. Experimental schematic for analysis of *in vivo* CTX-induced injury of TA muscles combined with injection of self-delivering siRNAs at 3 days post injury. n = 4 mice per group, 3 months old. **M**. Representative immunofluorescence images of MYOGENIN (green), LAMININ (grey), and Hoechst (blue) of TA-sections 5 days post-injury from young mice (3 months old). **N.** Quantification of the number of Myogenin+ cells normalized per area. Unpaired t-test; *: p-value ≤ 0.05. **O.** Illustration of the experimental setup. Primary myoblasts

297 isolated from individual mice stably overexpressing (OE) LMOD1 (purple) or GFP (green) were seeded and either
298 collected during proliferation (3d proli), after 1 day (1d diff), 3 days (3d diff) or 5 days (5d diff) of differentiation.
299 Differentiation was induced by a change to differentiation medium at 0h. Cells were harvested for
300 immunofluorescence analysis (IF), qRT-PCR, immunoblot (WB) or mass spectrometry (MS). **P.** Representative
301 immunofluorescence images of primary myoblasts after one day of differentiation, showing either stable expression
302 of LMOD1 or GFP. devMHC (green), MYOGENIN (red) and nuclei (blue). Scale bar is 50 µm. **Q** and **R.**
303 Quantification of nuclei per myotube of GFP OE or LMOD1 OE cells (**Q**) and cells expressing Myogenin+/MHC+
304 defined as just differentiated cells (**R**) after 1 day of differentiation. Paired t-test *: p-value ≤ 0.05. Related to Figure
305 S2. In all bar plots, each symbol represents a biological replicate, and the error bars indicate the SD.
306

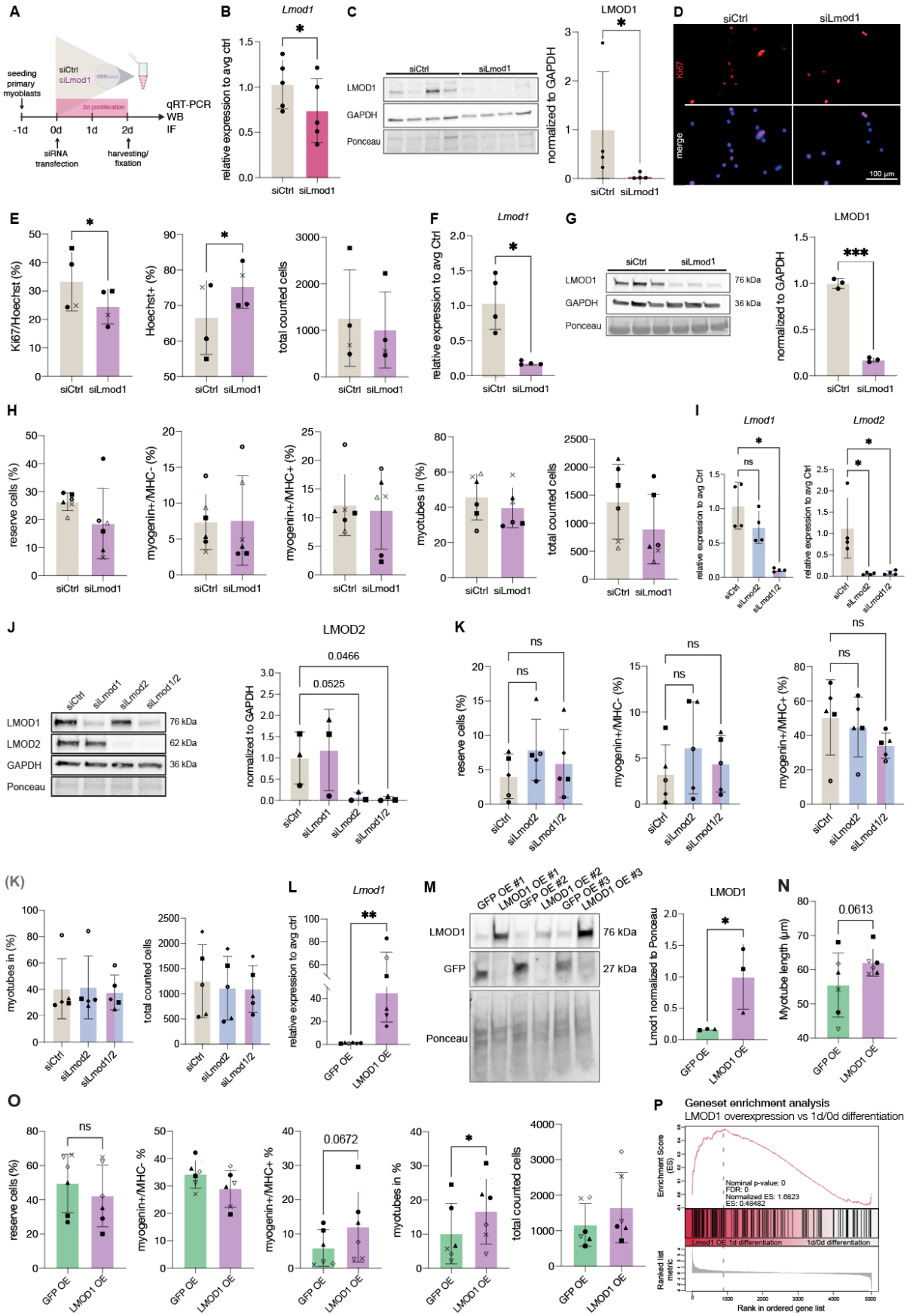

Figure S2: Validation of knockdown efficiency and statistical analysis of siLmod1/Lmod2 knockdown and LMOD1 overexpression

A. Schematic of the *Lmod1* knockdown experiment under proliferating conditions. siRNA directed against *Lmod1* or scramble (siCtrl) control was used to transfect primary myoblasts isolated from individual mice. **B.** qRT-PCR analysis showing the relative expression of *Lmod1* after siLmod1 knockdown compared to siCtrl transfected cells, normalized to *Gapdh* expression levels. **C.** Immunoblot and quantification of LMOD1 after transfections with siLmod1 and siCtrl and two days of proliferation normalized to GAPDH. Paired t-test: *: p-value ≤ 0.05. **D.** Immunofluorescence analysis of primary myoblasts stained for the proliferation marker Ki67 (red) and Hoechst (blue). Scale bar: 100 µm. **E** Quantification of cell populations identified by immunofluorescence staining: reserve cells being Hoechst+/Ki67- and cells being Hoechst+/Ki67+ in siCtrl and siLmod1 transfected conditions and the total counted cells per condition. **F.** and **G.** Validation of the siLmod1 knockdown compared to siCtrl transfected cells under differentiation conditions. qRT-PCR for *Lmod1* normalized to *Gapdh* expression levels (**F**) and immunoblot analysis with quantification of LMOD1 signal normalized to GAPDH (**G**). Paired t-test *: p-value ≤ 0.05, ***. **H.** Quantification of cell populations identified by immunofluorescence staining: reserve (Hoechst+/Myogenin-/MHC-) cells, Myogenin+/MHC- cells, Myogenin+/MHC+, fully differentiated myotubes and total counted cells under differentiating conditions. **I.** and **J.** Validation of the *siLmod1* or *siLmod2* (single) or *siLmod1/Lmod2* (double) knockdown compared to siCtrl transfected cells under differentiation conditions. qRT-PCR for *Lmod1* and *Lmod2* normalized to *Gapdh* expression levels (**I**) and representative immunoblot with quantification of LMOD2 normalized to GAPDH (**J**). One-way ANOVA *: p-value ≤ 0.05 or numbers are indicated. ns: not significant. **K.** Quantification of cell populations (in %) identified by immunofluorescence staining after siLmod1 (single), siLmod2 (single) and siLmod1/2 (double) knockdown under differentiating conditions: reserve (Hoechst+/Myogenin-/MHC-) cells, Myogenin+/MHC- cells, Myogenin+/MHC+, fully differentiated myotubes and total counted cells under differentiating conditions. Related to Figures 3I and 3J. **L** and **M.** Validation of LMOD1 OE compared to GFP OE cells after one day of differentiation. Relative *Lmod1* expression assessed by qRT-PCR was compared to GFP OE cells and normalized to *Gapdh* expression levels (**L**) and immunoblot with quantification of LMOD1 normalized to GAPDH (**M**). Paired t-test: *: p-value ≤ 0.05. **N** and **O.** Quantification of cell populations identified by immunofluorescence staining after LMOD1 OE compared to GFP OE: reserve (Hoechst+/Myogenin-/MHC-) cells, Myogenin+/MHC- cells, Myogenin+/MHC+, fully differentiated myotubes, total counted cells after and myotube length (in µm) (**N**). Paired t-test: numbers are indicated, ns: not significant. Related to Figures 3N and 3O. **P.** Gene set enrichment analysis (GSEA) was based on a gene set containing proteins that significantly increased at one day of differentiation compared to 0h/proliferating primary myoblasts (AVG Log2 Ratio > 0.58 and Q value < 0.05, 189 proteins) from the proteomic data generated in (Figure 1A). The GSEA was performed using this gene set on the comparison LMOD1 OE vs. GFP OE at 1 day of differentiation (Table S2). In all bar plots, each symbol or black dot represents a biological replicate, and the error bars indicate the SD.

LMOD1 interacts with SIRT1 and SIRT2

To elucidate the mechanism by which LMOD1 contributes to myogenic differentiation, we performed a proximity-dependent biotinylation experiment (BioID) for LMOD1 to identify its interaction partners in HEK293T cells (Figure 4A). Given their sequence similarity but distinct functions during myogenic differentiation, we analyzed the interaction partners of LMOD1 and LMOD2 in parallel and focused on hits retrieved exclusively by LMOD1. Therefore, we fused the promiscuous biotin ligase (BirA*) C-terminal to Lmod1 or Lmod2. A cell line expressing only the sequence for BirA* was used as a control (BirA*-Ctrl) to account for non-specific biotinylation. The tetracycline-dependent expression of the respective fusion proteins was validated by immunofluorescence (Figure 4B and 4C) and anti-FLAG immunoblot (Figure S3A). Biotinylation activity, after the addition of exogenous biotin, was assessed using streptavidin-HRP immunoblot (Figure S3A) and immunofluorescence staining (Figure 4B and 4C). Subsequently, biotinylated proteins were captured using streptavidin enrichment and analyzed by mass spectrometry (Table S3). PCA analysis demonstrated a distinct separation between C-terminal fused LMOD1 and LMOD2 expression constructs (Figure 4D). Using both

360 LMOD1 and LMOD2, we found a significant enrichment compared to the BirA*-Ctrl for known
361 interaction partners (Fowler and Dominguez 2017; Boczkowska et al. 2015) involved in actin
362 filament nucleation such as Tropomodulins (TMODs) and Tropomyosins (TPMs) (Figure S3B-
363 D), validating our constructs. Interestingly, a direct comparison of streptavidin-enriched
364 proteins from LMOD1-BirA* vs. LMOD2-BirA* revealed a subset of interaction partners that
365 specifically interact with LMOD1. These include the histone deacetylases sirtuin 1 (SIRT1)
366 and sirtuin 2 (SIRT2), as well as the RuvB Like AAA ATPase 1/2 (RUVBL1/2) (Figure 4E and
367 4F). Sirtuins are involved in various biological processes, including DNA regulation,
368 metabolism, longevity, and myogenesis (Horio et al. 2011; Abdel Khalek et al. 2014;
369 Vachharajani et al. 2016). In particular, one study revealed that mice with muscle-specific
370 inactivation of Sirt1 displayed repression of the myogenic program (Ryall et al. 2015). Since
371 SIRT1 was already identified as a potential mediator of myogenesis, we wanted to validate its
372 preferential interaction with LMOD1 by co-immunoprecipitation independently. Therefore, we
373 transfected SIRT1 as a GFP fusion protein in HEK293T expressing LMOD1-BirA* or LMOD2-
374 BirA* and performed pull-down experiments using a GFP trap. Immunoblot analysis of the
375 GFP-trap eluates using anti-BirA antibodies confirmed a co-precipitation between LMOD1 and
376 SIRT1, while LMOD2 co-precipitated with SIRT1 to a lower extent (Figure 4G). To further
377 validate the interaction of LMOD1 and SIRT1 in primary myoblasts and myogenic
378 differentiation, we performed *in situ* detection of LMOD1 and SIRT1 using proximity ligation
379 assays (PLA) (Figure 4H). In proliferating myoblasts, when the abundance of LMOD1 is low,
380 only a weak PLA signal indicating close proximity of SIRT1 and LMOD1 was detectable both
381 in the cytoplasm and the nucleus. However, at the beginning of myogenic differentiation, when
382 the abundance of LMOD1 increases, an increase in PLA signals indicating close proximity of
383 LMOD1 and SIRT1 was detectable almost exclusively in the cytoplasm. Together these data
384 show that LMOD1 preferentially interacts with the deacetylase SIRT1, suggesting a potential
385 functional interaction between these two proteins in modulating myogenic differentiation.
386
387

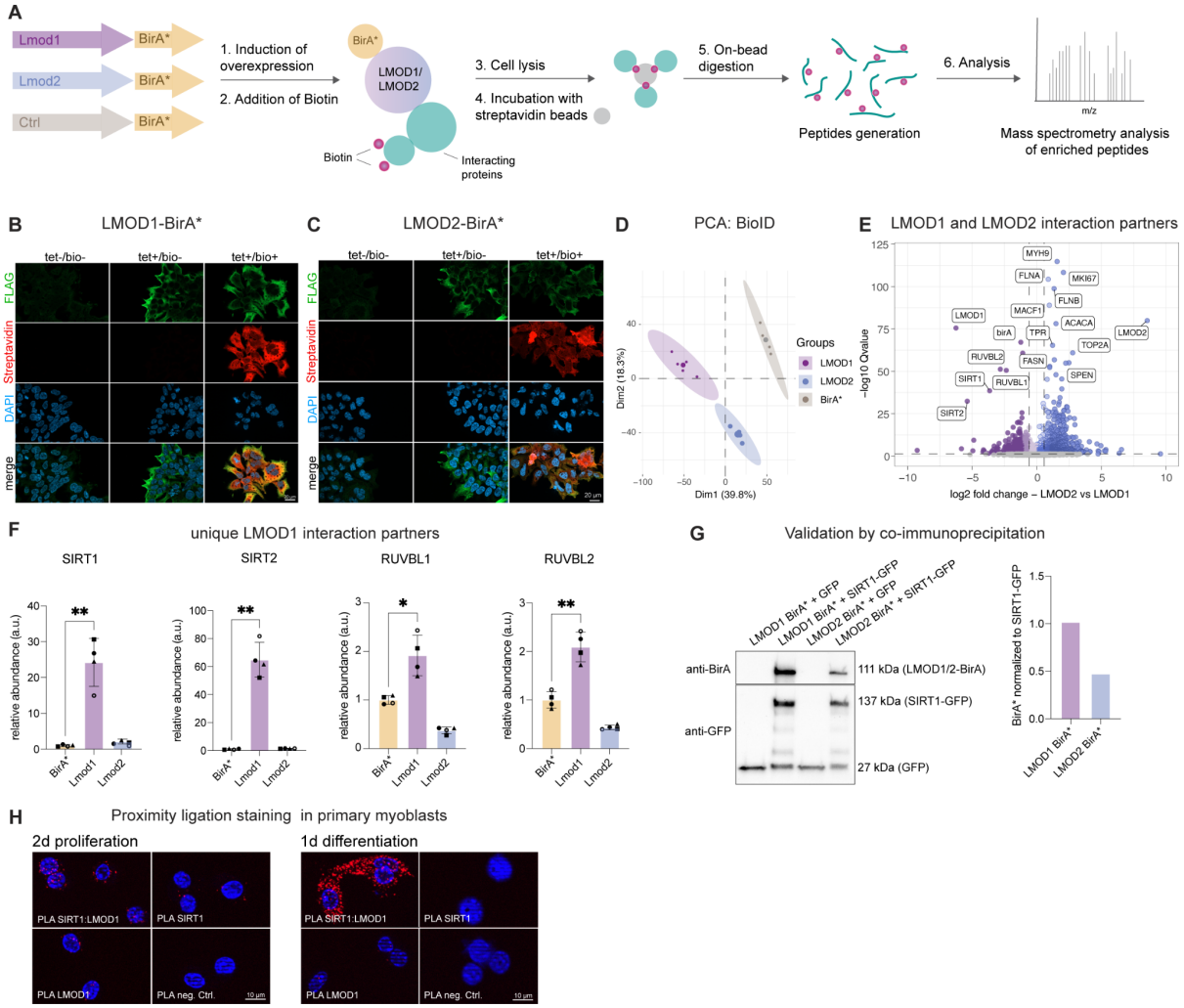

Figure 4: LMOD1 interacts with SIRT1

A. BioID workflow. Lmod1 and Lmod2 were C-terminally fused to a promiscuous biotin ligase (BirA*) and expressed in HEK293T cells. BirA* alone served as a control (Ctrl) to assess non-specific biotinylation. Overexpression of fusion proteins was induced by addition of tetracycline. Exogenous biotin was introduced to label interaction partners in close proximity. Biotinylated proteins were captured using streptavidin enrichment, followed by mass spectrometry analysis to identify and quantify proximal interactors. **B.** and **C.** Immunofluorescence analyses of LMOD1-BirA*-FLAG and LMOD2-BirA*-FLAG in HEK293T cells 4 days after seeding without addition of any substance (-tet/-bio), with addition of only tetracycline for 4 days (+tet/-bio) or with addition of both tetracycline for 4 days and biotin for 1 day (+tet/+bio); FLAG (green), Streptavidin (red), nuclei (blue). Scale bar: 20 µm. **D.** Principal component analysis (PCA) of the BioID data. Ellipses represent 95 % confidence intervals. **E.** Volcano plot of proteins enriched by streptavidin pull-down and analyzed by mass spectrometry from LMOD1-BirA* and LMOD2-BirA*. n = 4 biological replicates (Table S3) **F.** Quantification of selected unique interaction partners of LMOD1-BirA* and LMOD2-BirA* in comparison to BirA*-Ctrl. Each symbol represents a biological replicate, error bars indicate the SD. One-way ANOVA, *: p-value ≤ 0.05, **: p-value ≤ 0.01. **G.** Validation of the SIRT1-LMOD1 interaction. Cells expressing either GFP or SIRT1-GFP were used for co-immunoprecipitation using GFP-trap. The eluates from the GFP-trap were analyzed by immunoblot using antibodies directed to BirA* or GFP. For quantification, BirA* was normalized to SIRT1-GFP intensity. **H.** Representative images of proximity ligation assay (PLA) (red) in primary myoblasts during proliferation and after one day of differentiation. Scale bar: 10 µm.

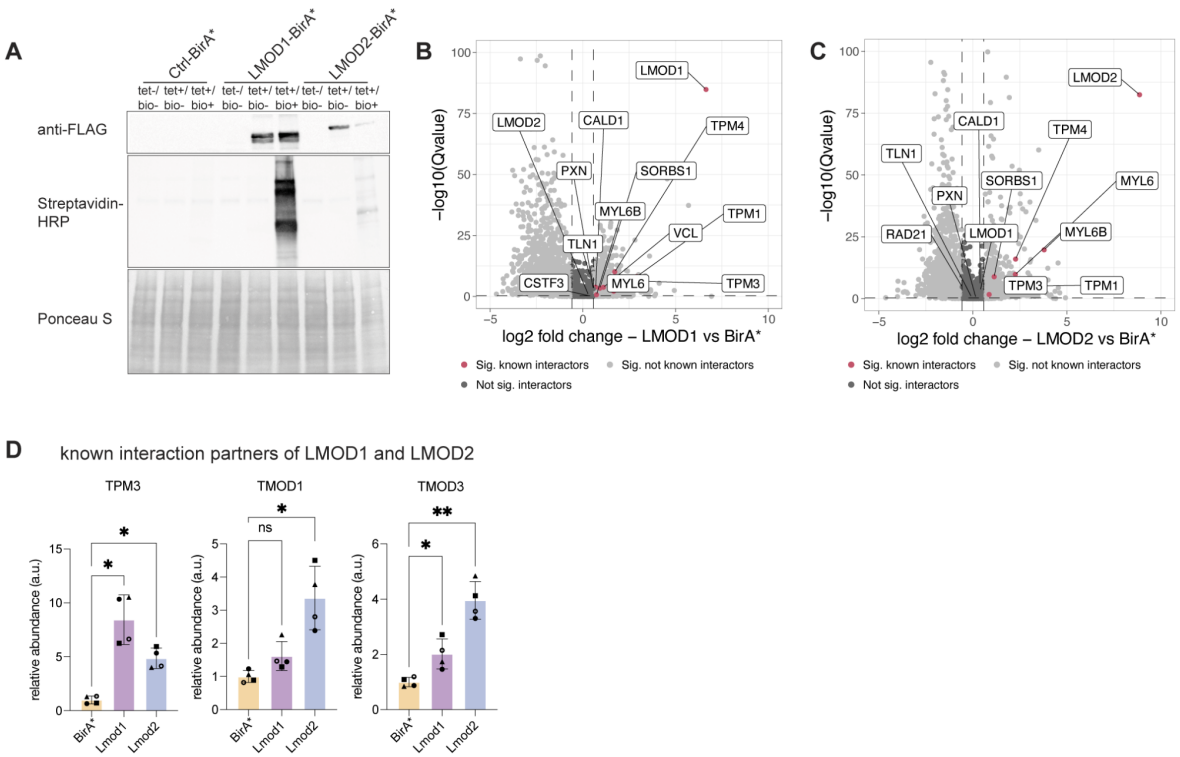

Figure S3: BioID for LMOD1 and LMOD2

A. Immunoblot of BirA* fusion proteins performed on lysates from HEK293T cells stably transfected with LMOD1-BirA*-FLAG, LMOD2-BirA*-FLAG or Ctrl-BirA*-FLAG following 24 h incubation with (+tet) or without (−tet) tetracycline. Middle panel, streptavidin-HRP blot following induction of BirA* fusion proteins with tetracycline and supplementation of biotin for 24 h. Ponceau stainings were used as loading control. HRP: horseradish peroxidase. **B**. Volcano plot of proteins enriched by streptavidin pull-down and analyzed by mass spectrometry from LMOD1-BirA* and **C.** LMOD2-BirA* compared to BirA*-Ctrl. Significantly enriched (AVG Log2 Ratio > 0.58 and Q value < 0.05), known interaction partners for LMOD1 and LMOD2 are highlighted in red (Table S3). **D.** Quantification of selected known interaction partners of LMOD1-BirA* and LMOD2-BirA* in comparison to BirA*-Ctrl. Each symbol represents a biological replicate, and error bars indicate the SD. One-way ANOVA, *: p-value ≤ 0.05, **: p-value ≤ 0.01.

LMOD1 and SIRT1 show dynamic subcellular localization during myogenic differentiation

Next, we investigated how LMOD1 might influence SIRT1 activity and thereby myogenic differentiation. SIRT1 has been shown to localize both in the cytoplasm and nucleus of neural precursor cells, murine pancreatic beta cells, rat cardiomyocytes, and vascular endothelial cells, while LMODs have been mainly associated with cytoplasmic localization (Hisahara et al. 2008; Tanno et al. 2010; Tong et al. 2013; Tanno et al. 2007; Conley 2001; Nauen et al. 2020). To determine the localization of SIRT1 and LMOD1 and a potential change in localization during myogenesis, we performed co-immunostainings for LMOD1 and SIRT1 in primary myoblasts to determine their localization at different stages of myogenic differentiation (Figure 5A). Overall, the total fluorescence intensity of LMOD1 significantly increased during differentiation (Figure S4A), while the signal intensity of SIRT1 slightly decreased (Figure S4B). However, under proliferating conditions, SIRT1 and LMOD1 predominantly localized in

434 the nucleus (Figure 5A). Interestingly, after initiation of differentiation, both SIRT1 and LMOD1
435 were clearly detectable in the cytoplasm, indicating their translocation into the cytoplasm. At
436 a later time point (2d of differentiation), the localization of SIRT1 can once again be observed
437 in the nucleus, while LMOD1 remains in the cytoplasm. Using the fluorescent signal intensity,
438 we quantified the cytoplasmic/nuclear ratios for both SIRT1 and LMOD1 and found that both
439 proteins change their intracellular distribution during myogenic differentiation suggesting that
440 their localization in the cell affects the differentiation process (Figures 5B and 5C). Of note, we
441 also observed a correlation between their cytoplasmic-nuclear partitioning, particularly during
442 proliferation and at day one of differentiation (Figure 5D and 5E). The correlation between their
443 respective localization was reduced at day 2 of differentiation, with SIRT1 displaying mainly a
444 nuclear localization while LMOD1 remained predominantly cytoplasmic (Figure 5F). We
445 confirmed these dynamic changes of sub-cellular localization for SIRT1 and LMOD1 by
446 cellular fractionation experiments followed by immunoblot analysis (Figure S4C).
447 Since SIRT1 protein abundance decreased with each day of differentiation as shown by our
448 proteomics data and immunoblot analysis (Figure 5G and S4D), we hypothesized that the
449 LMOD1-mediated change in SIRT1 location is especially required during early differentiation.
450 Therefore, we repeated the cellular fractionation experiments focusing on the onset of
451 myogenic differentiation with additional time points and by using LMOD1 OE cells. Next, we
452 compared the nuclear fraction of the LMOD1 OE cells to the control cells to determine if
453 LMOD1 alone can alter SIRT1 subcellular localization (Figure 5H-K). In particular, at 6 and 12
454 hours of differentiation, SIRT1 is highly abundant in the nucleus in control cells. However,
455 these dynamics shift and the SIRT1 abundance decreases in the nucleus when LMOD1 is
456 overexpressed (Figure 5H and 5I). In line with this observation, in LMOD1 overexpressing
457 cells the cytoplasmic SIRT1 abundance increased at 0h (proliferation) and 6h differentiation,
458 suggesting a shift of SIRT1 protein to the cytoplasm upon LMOD1 OE compared to the control
459 already under proliferating conditions (Figure 5J and 5K). Together these data demonstrate
460 that SIRT1 and LMOD1 dynamically change their subcellular localization and that
461 overexpression of LMOD1 favors the cytoplasmic localization of SIRT1 at early stages of
462 myogenic differentiation.

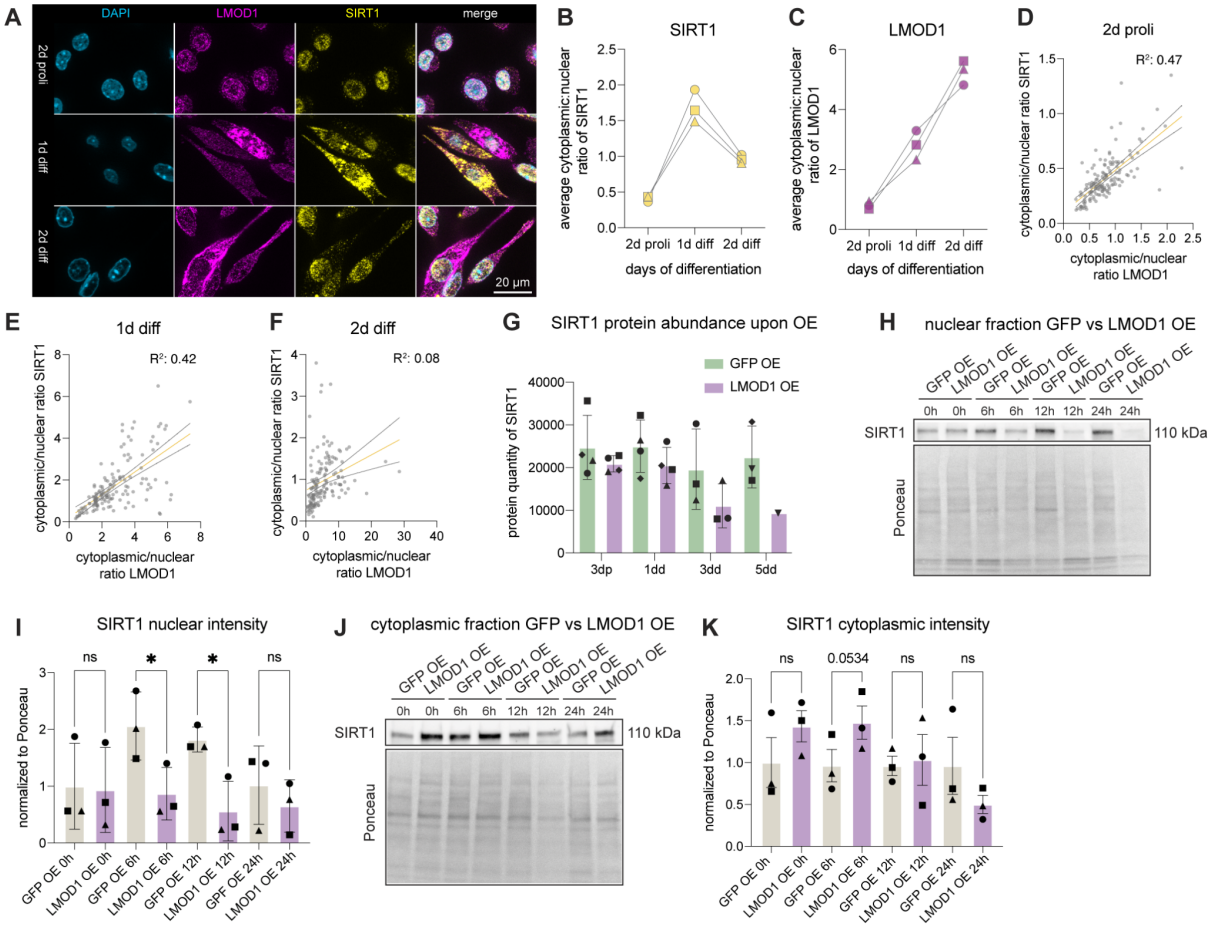

Figure 5: Overexpression of LMOD1 influences the subcellular localization of SIRT1.
A. Representative immunofluorescence staining of LMOD1 and SIRT1 at different timepoints of myogenic differentiation; LMOD1 (purple), SIRT1 (yellow), nuclei (Hoechst, blue). Scale bar: 20 µm. **B - C.** Cytoplasmic to nuclear SIRT1 (**B**) and LMOD1 (**C**) ratio at different days of differentiation, n = 50 cells were analyzed per biological replicate per time point. **D - F.** Correlation of the cytoplasmic to nuclear ratio of LMOD1 and SIRT1 at 2 days of proliferation (R^2 = 0.47) (**D**), 1 day differentiation (R^2 = 0.42) (**E**) and 2 days of differentiation (R^2 = 0.08) (**F**). **G.** SIRT1 protein abundance upon LMOD1 OE at different timepoints, 3 days proliferation (3dp), 1 day differentiation (1dd), 3 days differentiation (3dd), 5d differentiation (5dd). Each symbol represents a biological replicate (n = 4, primary myoblasts); error bars indicate SD. **H - K.** Representative immunoblot of SIRT1 in the nuclear (**H** and **I**) and cytoplasmic (**J** and **K**) fraction, comparing GFP and LMOD1 OE at early time points of differentiation (0h: undifferentiated/proliferating, 6h, 12h, 24h of differentiated primary myoblasts). SIRT1 signal was analyzed in n = 3 immunoblots and was normalized to Ponceau. In bar plots, each symbol represents a biological replicate, and the error bars indicate the SD. Paired t-test *: p-value ≤ 0.05, ns: not significant.

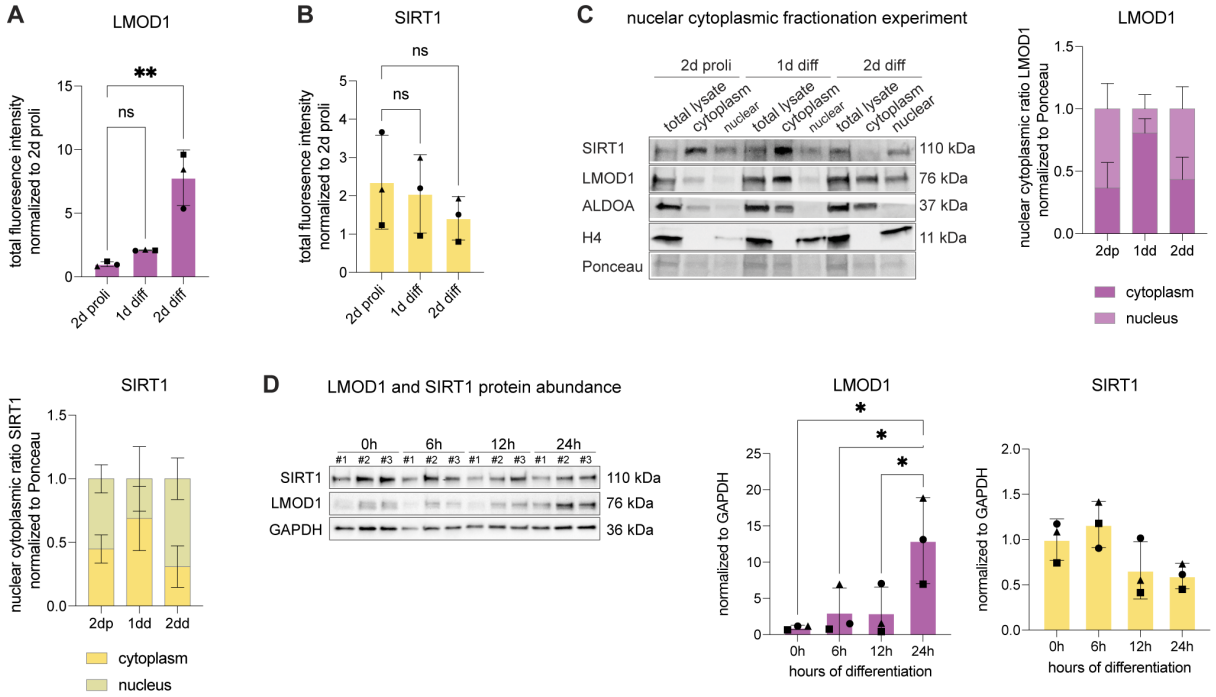

Figure S4: Sub-cellular localization of LMOD1 and SIRT1 during myogenic differentiation
A - B. Total immunofluorescence intensity (nucleus and cytoplasm) of LMOD1 (**A**) and SIRT1 (**B**) during different timepoints of myogenic differentiation. **C.** Representative immunoblot of the nuclear-cytoplasmic fractionation experiment in primary myoblasts at different timepoints: 2d proliferation, 1d differentiation and 2d differentiation. SIRT1 and LMOD1 signal was analyzed in (n = 3) immunoblots and was normalized to Ponceau. ALDOA signal was used as a cytoplasmic marker, and Histone 4 (H4) was used as a nuclear marker. Immunoblot analyses of LMOD1 and SIRT1 intensity for each cellular compartment are depicted in the barplots. One-way ANOVA *: p-value ≤ 0.05, ns: not significant. **D.** Immunoblot showing LMOD1 and SIRT1 protein abundance at different timepoints of myogenic differentiation (0h = proliferating conditions, 6h differentiation, 12h differentiation, 24h differentiation). Quantification of immunoblots for LMOD1 and SIRT1 shown in barplots normalized to GAPDH. For all bar plots, each symbol represents a biological replicate, and the error bars indicate the SD.

Reduction or inhibition of SIRT1 can partially restore the impaired myogenic differentiation caused by knockdown of LMOD1

Given the interaction of LMOD1 and SIRT1, we hypothesized that LMOD1 regulates SIRT1-mediated transcription of genes that are critical for myogenic differentiation. To test this hypothesis, we investigated the impact of reduced SIRT1 levels using both a genetic (siRNA targeting *Sirt1*) and a pharmacological approach (25 µM EX527, small molecule inhibitor specific for SIRT1) during myogenic differentiation (Figure 6A) (Peck et al. 2010; Broussy, Laaroussi, and Vidal 2020). Primary myoblasts were transfected with siLmod1 and siSirt1 or incubated with EX527, at the time of induction of differentiation. After three days of differentiation, immunofluorescence staining was performed and analyzed (Figure 6B). We confirmed the significant decrease in LMOD1 and SIRT1 levels upon siRNA-mediated knockdown through immunoblot analysis (Figure S5A) and qRT-PCR (Figure S5B). Our results show that both genetic and pharmacological inhibition of SIRT1 signaling effectively promoted myogenic differentiation (Figure 6B and 6F) leading to an increased number of

507 nuclei per myotube in the siLmod1/siSirt1 double knockdown compared to the knockdown of
508 LMOD1 alone, indicating an improvement in myotube fusion after knockdown of SIRT1
509 (Figure 6C, 6G and Figure S5C and S5D). Moreover, both interventions were able to
510 counteract the negative effects observed after knockdown of LMOD1 alone (Figure 6D and
511 6H). Previous studies have demonstrated that *Sirt1* knockout mice exhibited premature
512 differentiation of MuSCs (Ryall et al. 2015). As a measure of myogenic differentiation, we
513 measured the length of myotubes and observed an elongation after knocking down SIRT1
514 together with LMOD1 (Figure 6E and 6I).
515 Next, we performed RNA-sequencing to identify downstream effectors that could explain the
516 improvements in myogenic differentiation observed after double knockdown of Lmod1 and
517 Sirt1 (Table S4). Therefore, we performed a knockdown of *Lmod1* and *Sirt1* two days prior to
518 differentiation, followed by a second siRNA transfection at the initiation of differentiation to
519 ensure a high knockdown efficiency. After one day of differentiation, cells were harvested to
520 quantify early transcriptional changes in the myogenic program after knockdown of *Lmod1*
521 and *Sirt1* using RNAseq (Figure 6J). Differential gene expression analysis confirmed a
522 significant reduction of *Lmod1* and *Sirt1* mRNA in our experimental setup (Figure S5E). Next,
523 we identified 246 genes being significantly and oppositely regulated after knockdown of either
524 *Lmod1* or *Sirt1* (Table S4). Interestingly, among these genes, we identified a subset of known
525 SIRT1 target genes that were previously defined by ChIP-Seq analysis of MuSCs from WT
526 and Sirt1^{mKO} mice (Ryall et al. 2015) (Table S4). These include key factors involved in cell
527 signaling and differentiation, such as *Fgf6*, *Tgfa*, *Mcr*, *Lifr*, and *Camk1d* (Figure 6K). Taken
528 together, our data show that genetic or pharmacological inhibition of SIRT1 signaling can
529 partially reverse the impaired myogenic differentiation caused by knockdown of Lmod1 and
530 that affecting LMOD1 level is sufficient to alter the expression of a subset of SIRT1 target
531 genes, highlighting the role of the LMOD1-SIRT1 axis in myogenic differentiation.

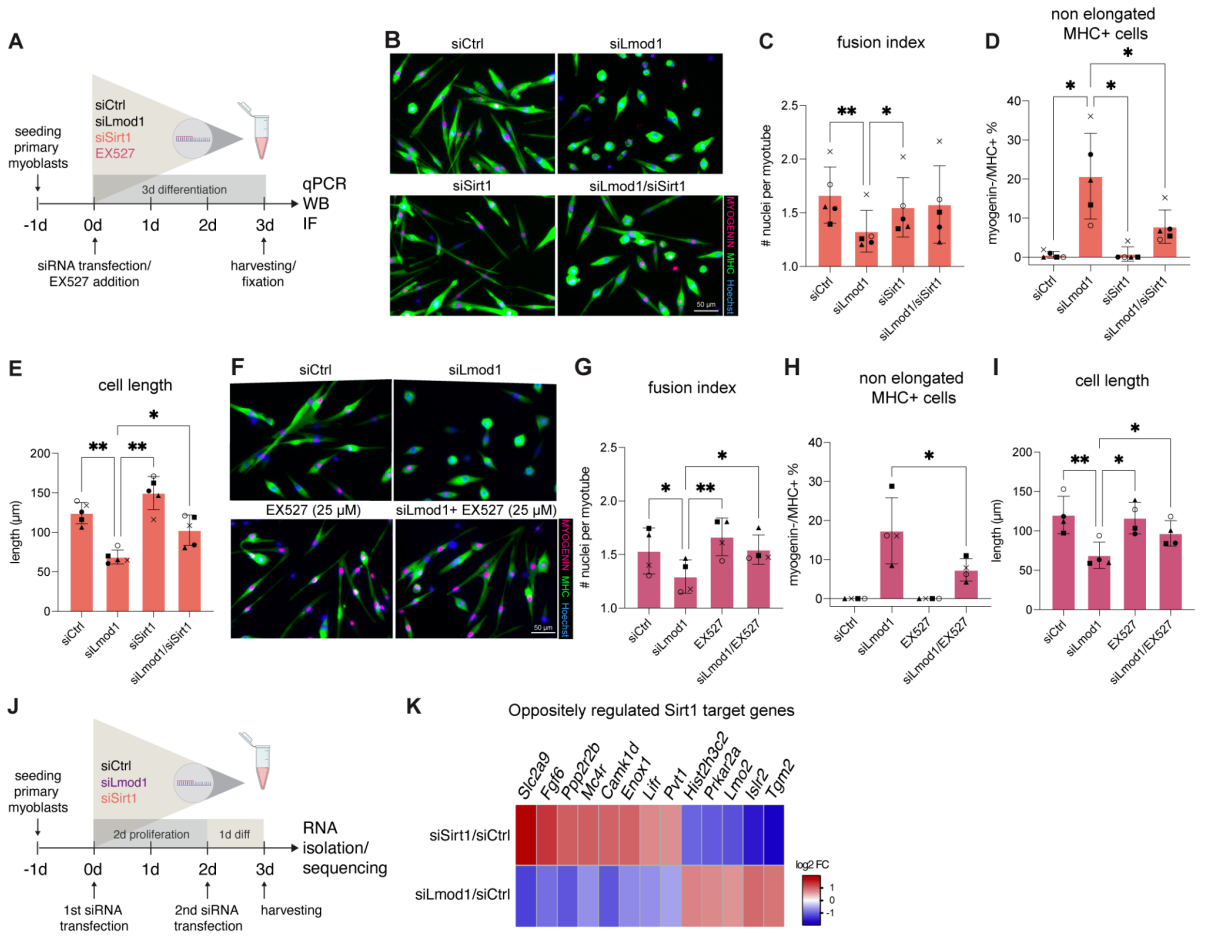

Figure 6: Reduced SIRT1 signaling can partially reverse siLmod1-induced impaired myogenic differentiation

A. Illustration of the experimental setup. Primary myoblasts were co-transfected with *Lmod1*-specific siRNA (siLmod1) and siRNA against Sirt1 (siSirt1) (depicted in orange) or treated with SIRT1 inhibitor EX527 (depicted in pink), simultaneously to the induction of differentiation. **B./F.** Representative immunofluorescence images after *Lmod1* and *Sirt1* knockdown with siRNA at day 3 of differentiation (**B**) or after *Lmod1* knockdown and addition of 25 µM EX527 at day 3 of differentiation (**F**); MYOGENIN (red), devMHC (green), nuclei (Hoechst, blue). **C - E.** Quantification of the number of nuclei per myotube (**C**), percentage of Myogenin-/MHC+ cells (**D**) and measured length of differentiated myotubes (**E**) after siRNA transfection of SIRT1 and LMOD1. One-way ANOVA *: p-value ≤ 0.05, **: p-value ≤ 0.01. **G - I.** Quantification of the number of nuclei per myotube (**G**), percentage of Myogenin-/MHC+ cells (**H**) and measured length of differentiated myotubes (**I**) after siRNA knockdown of LMOD1 and EX527 treatment to inhibit SIRT1. One-way ANOVA *: p-value ≤ 0.05, **: p-value ≤ 0.01. **J.** Illustration of the experimental setup for the RNA-Seq experiment. Primary myoblasts were first seeded and then transfected with siRNA against LMOD1 or SIRT1 or siCtrl. After two days of incubation, the primary myoblasts were transfected a second time with siRNA and induced to differentiate simultaneously. After one day of differentiation, cells were harvested, and RNA was isolated for library preparation and RNAseq analysis. **K.** Heatmap indicating oppositely differentially expressed SIRT1 target genes from siSirt1 vs siCtrl an siLmod1 vs siCtrl with a log2 FC ratio > 0.58. SIRT1 target genes identified from ChipSeq experiment published in (Table S4) (Ryall et al. 2015). For all bar plots, each symbol represents a biological replicate, and the error bars indicate the SD.

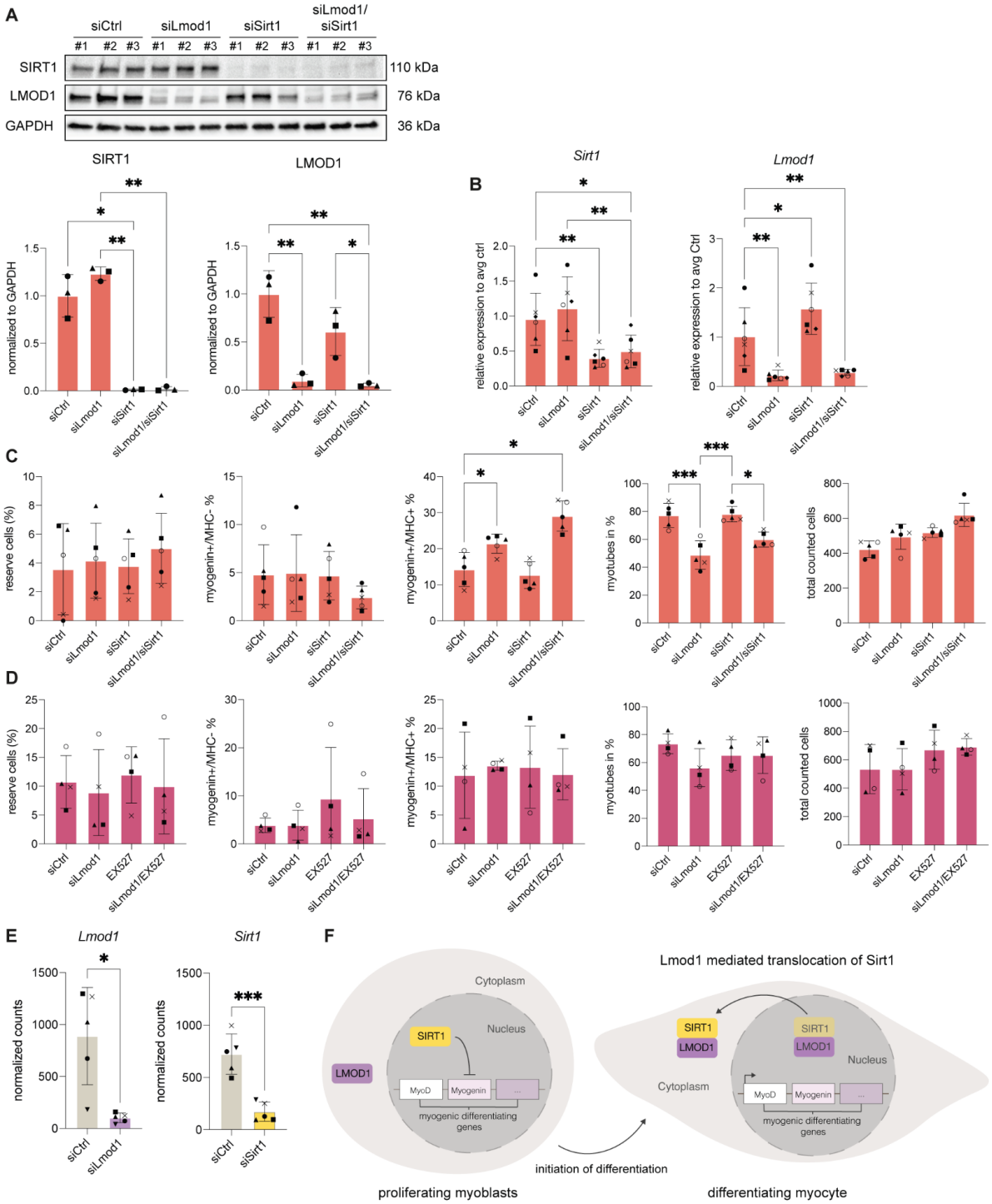

Figure S5: Reduced SIRT1 signaling can partially reverse siLmod1-induced impaired myogenic differentiation

A. Immunoblot validation of the LMOD1 and SIRT1 single knockdown and double knockdown (siLmod1/siSirt1) or a scrambled siRNA. Primary myoblasts were transfected at the initiation of differentiation and harvested after three days of differentiation. One-way ANOVA: *: p-value ≤ 0.05. **: p-value ≤ 0.01. **B.** qRT-PCR analysis showing the relative expression of *Sirt1* and *Lmod1* in siLmod1 or siSirt1 single knockdown or double knockdown compared to siCtrl treated cells, normalized to *Gapdh* expression levels. Paired t-test *: p-value ≤ 0.05 **: p-value ≤ 0.01. **C** and **D.** Percentage of cell populations found in immunofluorescence staining: reserve (Hoechst+/Myogenin-/MHC-) cells, Myogenin+/MHC- cells, Myogenin+/MHC+, fully differentiated myotubes and total counted cells under differentiating conditions after siRNA mediated knockdown of LMOD1 and SIRT1 (**C.** related to Figure 6C - E) or

siRNA mediated knockdown of LMOD1 and EX527 treatment to inhibit SIRT1 (**D.** related to Figure 6G - I.) **E.** Normalized RNA-seq read counts of *Lmod1* and *Sirt1* after one day of differentiation after siCtrl and siLmod1 and siCtrl and siSirt1 knockdown (Table S4). Paired t-test *: p-value ≤ 0.05 ***: p-value ≤ 0.001. For all bar plots, each symbol represents a biological replicate, and the error bars indicate the SD. **F.** Working model: During the proliferation stage, SIRT1 is found in the nucleus, repressing the expression of myogenic regulating factors. However, at the onset of myogenic differentiation, LMOD1 interacts with SIRT1 and affects its subcellular localization, leading to decreased levels of SIRT1 in the nucleus. This reduction in SIRT1 levels results in the de-repression of MRFs and the initiation of differentiation.

573 **Discussion**

574 Myogenic differentiation involves the coordinated alterations of gene expression and
575 reorganization of the cellular architecture. Here, we present a temporally resolved analysis of
576 the proteome of primary mouse myoblasts undergoing differentiation *in vitro.* With a depth of
577 more than 6000 proteins, our analysis covers three times more proteins compared to a
578 previous study performed on an immortalized myoblast cell line (C2C12 cells) (Tannu et al.
579 2004; Kislinger et al. 2005). By using five independent primary myoblast lines, we were able
580 to take into account the variability that typically affects primary cultures and derive robust and
581 reproducible proteome signatures (Hindi et al. 2017; K. H. Kim, Qiu, and Kuang 2020). Our
582 data highlight hundreds of changes in energy metabolism, RNA and protein synthesis as well
583 as cytoskeletal organization that occur with specific temporal dynamics during myogenic
584 differentiation. To demonstrate the relevance of our data, we decided to focus on LMOD1, a
585 cytoskeletal protein whose role in myogenic differentiation has not yet been investigated.
586 Although it is known that actin cytoskeletal dynamics are involved in myogenesis and that
587 LMOD1 contributes to actin filament nucleation in smooth muscle cells (Guerin and Kramer
588 2009; Heng and Koh 2010; Xie et al. 2020; Chereau et al. 2008), the biological significance
589 and functional role of LMOD1 during myogenic differentiation remained so far elusive. We
590 found that LMOD1 is expressed by MuSCs, that its expression increases during myogenic
591 differentiation *in vitro* and *in vivo*, and that reduction of LMOD1 levels significantly affects
592 myotube formation and the number of myonuclei per myotube. Furthermore, the timing of
593 induction of LMOD1 expression during skeletal muscle regeneration suggests a role in
594 differentiation and fusion rather than in myofiber maturation. This is further supported by our
595 finding that knockdown of *Lmod*1 after injury of skeletal muscle results in reduced
596 regeneration. Consistently, our knockdown studies revealed that the reduction of LMOD1
597 severely affects the myogenic differentiation and myonuclear numbers. Cells that expressed
598 Myogenin started differentiating into proper myotubes, indicated by the quantification of
599 Myogenin+/MHC- and Myogenin+/MHC+ cells even after knockdown of LMOD1. However, a
600 subset of cells positive for MHC but negative for Myogenin did not progress in differentiation,
601 possibly due to loss or insufficient activation of myogenin expression. Loss of myogenin has
602 been shown to lead to deregulated mTORC1 signaling and results in faster cell cycle entry in
603 MuSCs (Ganassi et al. 2020). Since the knockdown of LMOD1 leads to an increase in the
604 percentage of Myogenin-/MHC+ cells, the observed differentiation phenotype might be at least
605 partially explained by a direct or indirect effect of LMOD1 on myogenin expression.

606 We found that LMOD1 selectively interacts with SIRT1. So far, there is no direct evidence
607 suggesting that LMOD1 and SIRT1 have a specific binding domain where they can directly
608 bind to each other. However, the comparison of primary sequences between LMOD1 and
609 LMOD2 (Fowler and Dominguez 2017) reveals a 103 amino acid sequence unique for LMOD1,

610 which could represent a possible binding interface. It is also conceivable that other proteins or
611 molecules might be involved in mediating the interaction between LMOD1 and SIRT1, e.g.,
612 the RuvB-like AAA ATPase 1/2 (RUVBL1/RUVBL2). RUVBL1 participates in various
613 complexes, including INO80, NuA4, SWR1, TIP60-P400, PAQosome (R2TP), as a
614 transcriptional and/or chromatin modifier, with or without its homologue RUVBL2 (Gorynia et
615 al. 2011; P. B. Chen et al. 2015; Lakisic et al. 2016).
616 SIRT1 is a protein deacetylase that can localizes in the nucleus and cytoplasm (Bai and Zhang
617 2016; Moynihan et al. 2005; I.-Y. Chen et al. 2006), and was shown to play a critical role in
618 muscle differentiation and metabolism (Ryall et al. 2015; Diaz-Ruiz et al. 2015; Fulco et al.
619 2003, 2008). Myogenesis involves the shuttling of various proteins and myogenic regulators
620 between the nucleus and cytoplasm, regulated by various signals and interactions (Grifone et
621 al. 2021; Nguyen et al. 2022). We have observed that the localization of SIRT1 changes
622 dynamically during myogenic differentiation, and that the interaction between SIRT1 and
623 LMOD1 increases during the initial stages of myogenic differentiation. Additionally, we showed
624 that overexpression of LMOD1 affects the subcellular localization of SIRT1, leading to reduced
625 levels of SIRT1 in the nucleus. We hypothesize that relocation of SIRT1 to the cytoplasm,
626 mediated by LMOD1, is critical for the initiation of myogenic differentiation, resulting in the de-
627 repression of MRFs including myogenin. Alternatively, LMOD1 might sequester SIRT1 within
628 the cytoplasm, preventing its re-entry into the nucleus, which in turn results in the expression
629 of MRF to initiate myogenic differentiation (Figure S5F).
630 Previous studies have demonstrated that reducing the protein levels of SIRT1 can enhance
631 the differentiation of MuSCs (Ryall et al. 2015). Consistently, our data suggest that the
632 negative impact of knockdown of *Lmod1* on myogenic differentiation can be partially restored
633 by co-depletion of *Sirt1*. Our RNAseq analysis highlighted a subset of genes which were
634 oppositely up- or downregulated after knockdown of either LMOD1 or SIRT1, including
635 secreted factors and receptors that could potentially mediate this restoration of myogenic
636 differentiation when LMOD1 and SIRT1 levels are reduced. The identified factors include *Fgf6*,
637 *Tgfa*, *Camk1d*, *Mcr*, *Lifr*, *Isl2* and *Tgm2,* which were previously shown to be involved in
638 proliferation and differentiation of MuSCs (Armand, Laziz, and Chanoine 2006; Knight and
639 Kothary 2011; Yamane et al. 1998; Dos Santos et al. 2023; Hunt et al. 2013) by modulating
640 signaling pathways such as mTOR, Wnt or IGF1-PI3K/Akt-Foxo signaling (Wang et al. 2022;
641 Cui et al. 2020; Zhang et al. 2018). Further investigation of possible downstream effectors or
642 modulators identified by RNAseq could reveal additional mechanisms by which LMOD1
643 interferes with the myogenic program.
644 Finally, we have discovered that the abundance of LMOD1 is approximately four times higher
645 in MuSCs from geriatric mice compared to the abundance in MuSCs from young mice.
646 Specifically, LMOD1 tends to accumulate in the nucleus of MuSCs as mice age. Disruption of

647 the actin organization of the cytoskeleton and dynamics in aging and disease such as
648 Duchenne muscular dystrophy (DMD) or Nemaline myopathy (NM) were shown to impact the
649 expression of myogenic regulators and different signaling pathways (Lai and Wong 2020;
650 Eliazer et al. 2019; Y. J. Kim et al. 2022). Studies have shown that SIRT1 maintains H4K16 in
651 a deacetylated state in quiescent MuSCs, which leads to transcriptional repression (Ryall et
652 al. 2015). Given the SIRT1-LMOD1 interaction that we have discovered, we speculate that the
653 nuclear accumulation of LMOD1 might affect gene expression and chromatin remodeling in
654 aged MuSCs. However, it remains to be investigated whether the accumulation of LMOD1 is
655 a compensatory mechanism or is a causative factor leading to the dysregulation and
656 impairment of MuSCs during aging. Identifying the molecular mechanism and potential
657 downstream targets could be a promising strategy for discovering potential therapeutic targets
658 for promoting muscle regeneration and improving muscle health in older adults.

Acknowledgments

The authors gratefully acknowledge support from the FLI Core Facilities Proteomics, Sequencing, Imaging, and the Mouse Facility. A.O. is supported by the German Research Council (Deutsche Forschungsgemeinschaft, DFG) via the Research Training Group ProMoAge (GRK 2155), the Else Kröner Fresenius Stiftung (award number: 2019_A79), the Fritz-Thyssen Foundation (award number: 10.20.1.022MN), the Chan Zuckerberg Initiative Neurodegeneration Challenge Network (award numbers: 2020-221617, 2021-230967 and 2022-250618), and the NCL Stiftung. J.vM. received funding from the Deutsche Forschungsgemeinschaft (MA-3975/2-1), the Deutsche Krebshilfe and the Carl Zeiss Foundation (DKH-JvM-861005). S.C.S. was supported by a postdoctoral fellowship by the German Research Foundation (DFG, 505064275). The FLI is a member of the Leibniz Association and is financially supported by the Federal Government of Germany and the State of Thuringia.

Author contributions

Conceptualization: ES, SCS, JvM, AO
Data curation: ES, SCS, AO
Investigation: ES, IH, MH, AM, JvM
Methodology: ES, SCS, TD, JvM
Project administration: JvM, AO
Data analysis: ES, MH, AO
Supervision: JvM, AO
Visualization: ES, AO
Writing – original draft: ES, JvM, AO
Writing – review & editing: SCS

Declaration of interest

Authors declare no competing interests.

701 **EXPERIMENTAL MODEL AND SUBJECT DETAILS**
702
703 **Mice**
704 All wild-type mice were C57BL/6J obtained from Janvier or internal breeding at the Leibniz
705 Institute on Aging – Fritz Lipmann Institute (FLI) using the Janvier strain. All animals were kept
706 in groups in a specific pathogen-free animal facility with a constant 12 h light/dark cycle and
707 fed *ad libitum*. Young mice were aged 2-6 months, old mice were aged 18-20 months and
708 geriatric animals were aged 24-33 months. All animal experiments were approved by the
709 Thüringer Landesamt für Verbraucherschutz (Germany) under Reg.-Nr. FLI-17-014 and FLI-
710 22-011.
711
712 **Cardiotoxin muscle injury and siRNA injection of the TA muscle**
713 Young mice (3-months old) were anaesthetized by inhaling isoflurane using the Tec 7
714 Isoflurane (798932, Covetrus) Anesthesia Vaporizer (Datex Ohmeda). The TA muscle was
715 injured once by injecting 50 µl of 10 µM cardiotoxin (L8102, Latoxan) in sterile 0.9% NaCl
716 (12391112, Medpex) using an insulin syringe with a 29 G needle. To manage pain, the mice
717 were given Metacam (1 mg/kg, 798932, Covetrus) subcutaneously for three days.
718 Self-delivering Accell siRNA ON-TARGETplus Non-targeting Pool (D-001910-10-50,
719 Dharmacon) or Accell siRNA ON-TARGETplus targeting *Lmod1* (E-051082-00-0050,
720 Dharmacon) were injected into the CTX-damaged TA-muscles on day 3 after injury to induce
721 knockdown *in vivo*. TA muscles were further analyzed by quantifying the number of myogenin+
722 cells per area.
723
724 **FACS isolation of MuSCs**
725 MuSCs were isolated from the hindlimb muscles of adult male mice of age 8 - 12 weeks. The
726 muscles were dissected and collected in PBS, minced using scissors and digested in 2.5 g/mL
727 collagenase B (Sigma) and 1 g/mL dispase (Sigma) for 30 min at 37 °C. Together with 12 mL
728 of isolation medium (HAMs F10 + 20 % FBS) the digested muscle pieces were transferred
729 into a 15 mL tube to allow the sedimentation of larger undigested muscle chunks. The sample
730 was then filtered using a 0.74 mm cell strainer into a 50 mL tube, spun down at 450x *g* for 5
731 min at room temperature and resuspended in 500 mL isolation medium. The sample was then
732 incubated on ice for 15 min with the antibodies used for FACS analysis, as indicated below.
733 Afterwards, 15 mL PBS was added, and the sample was spun down for 5 min at 450x *g* at
734 room temperature followed by resuspension in 1mL PBS. After filtering the cells with a
735 0.35 mm cell strainer staining with SYTOX Blue Dead Cell Stain (S34857, Thermo Fisher) was
736 performed to distinguish between dead and alive cells. A BD FACSAria III was used for sorting
737 the cells. To FAC sort MuSCs, gating was set to alpha7-integrin+ (anti-Alpha 7 Integrin 647

738 (clone:R2F2), 67-0010-05, The University Of British Columbia AbLab, 1:500), CD11b-(CD11b-
739 PE, 553311, BD Bioscience, 1:500), CD31- (CD31-PE, 553373, BD Bioscience,1:500), CD45-
740 (CD45-PE, 553081, BD Bioscience,1:500) and Sca1- (Ly-6A/E-PE, 553108, BD Bioscience,
741 1:500).
742
743 **Cell culture**
744 FACS isolated primary myoblasts were cultured on collagen (#354236, Corning) coated (1h
745 at RT with 0.167 mg/mL) plates in Ham's F-10 Nutrient Mix (Thermo Fisher #31550031)
746 supplemented with 10 % FBS (#10270106, Thermo Fisher), 1 % Penicillin-Streptomycin
747 (#15140-122, Thermo Fisher) and 2.5 ng/mL bFGF (#13256029, Thermo Fisher) in a 37 °C
748 incubator with 95 % humidity and 5 % CO_2. For the proliferation assay, primary myoblasts
749 were seeded onto collagen-coated 24-well plates (734-2325, VWR) (25,000 cells per well) and
750 cultured for 48 h in the myoblast growth medium. For differentiation assays on 24-well plates,
751 75,000 primary myoblasts were seeded and cultivated for 72 h in the differentiation medium.
752 Primary myoblasts were always harvested using 0.25 % Trypsin. For location stainings, cells
753 were grown on collagen-coated 4-well culture slides (80426, Ibidi). For proliferation conditions,
754 5,000 cells were seeded per well, and 12,000 cells were seeded per well for differentiation
755 conditions. The cells were then incubated at 37 °C.
756 HEK293T cells (Flp-In 293 T-Rex cells) were obtained from Thermo Fisher (R78007).
757 HEK293T cells were grown in Dulbecco's modified Eagle's medium (#D6429, Sigma) with high
758 glucose (5 g/l) supplemented with 10 % heat-inactivated FBS and supplementation with 100
759 mg/mL Zeocin (#R250-01, Thermo Fisher) and 15 mg/mL Blasticidin (#R210-01, Thermo
760 Fisher). After generation of a stable line cells were supplemented with 100 mg/mL Hygromycin
761 (#10687-010, Thermo Fisher) and 15 mg/mL Blasticidin. Cells were cultured in a 37 °C
762 incubator with 95 % humidity and 5 % CO_2. For immunofluorescence staining of HEK293T,
763 cells were grown on 50 µg/mL Poly-D-Lysine solution (Gibco™ A3890401) coated autoclaved
764 coverslips (Carl Roth, YX03.1). Each coverslip was placed in an individual well of a 12-well
765 Lab solute plate (with a specified number), and 25,000 cells were seeded per well.
766 The Platinum-E (Plat-E) cells, a potent retrovirus packaging cell line were cultured in DMEM
767 high glucose (#D6429, Sigma) supplemented with 10 % FBS, 1 %Penicillin-Streptomycin in a
768 37 °C incubator with 95 % humidity and 5 % CO_2.
769
770 **siRNA transfection of cells with Lipofectamine® RNAiMAX Reagent**
771 Knockdown experiments using small interfering RNAs (siRNA) (ON-TARGETplus Non-
772 targeting Pool (D-001810-10-05, Dharmacon), SMART:pool ONTARGETplus Lmod1 siRNA
773 (9530015K06Rik | SM-Lmod), SMART:pool ONTARGETplus Lmod2 siRNA (C-Lmod),
774 SMART:pool ONTARGETplus Sirt1 siRNA (AA673258 | SIR2L1 | Sir2 | Sir2a | Sir2alpha)

775 against a target mRNA were performed. For siRNA transfection, the Lipofectamine®
776 RNAiMAX Kit (13778075, ThermoFisher) was used according to the manufacturer's protocol.
777
778 **Generation of overexpression cell lines**
779 The murine stem cell virus (MSCV) retroviral expression system (634401, Takarabio) was
780 used for overexpression studies. The MSCV vectors are optimized for introducing and
781 expressing target genes in stem cells such as MuSCs. The vector pENTR233.1-Lmod1
782 (100016603, Dharmacon, spectinomycin resistant) and GFP were blunt end cloned in the
783 donor vector cloneJET™ (K1232, Thermo Fisher, ampicillin-resistant) to finally generate
784 pMSCV.puro plasmids (634401, Takarabio, ampicillin-resistant) encoding Lmod1 and GFP,
785 respectively (Table 1).
786 Plat-E cells were transfected with 20 µg of the generated pMSCV.puro plasmids using
787 polyethylenimine (PEI). 60 uL PEI (1 mg/mL) were added to the plasmid mixture (3:1 ratio of
788 PEI:DNA), briefly mixed by inverting the tube and incubated for 20 min at RT. Subsequently,
789 the transfection complex was added dropwise to a 10 cm plate and incubated for 5-6 h in 3.5
790 % CO2, 37 °C. The medium was changed to standard proliferation medium (DMEM, 10 %
791 FBS and 1 % Pen-Strep) and incubated until the next day to collect the retrovirus. For further
792 infection of primary myoblasts, 1 Mio cells were seeded in a p10 plate and infected using a
793 1:5 ratio of retrovirus to growth medium (F10, 20 % FBS, bFGF, 1 % Pen-Strep) mixed with 5
794 µl of Protamine Sulfate (8 µg/mL). Infection of primary myoblasts was repeated the next day
795 as previously described and incubated at 37 °C. After 48 h post-transfection, primary
796 myoblasts were selected with 1.25 µg/mL puromycin for up to one week. Medium was changed
797 every 2 - 3 days.
798
799 ***In vitro* proximity labeling for BioID protocol**
800 HEK293T cells (Flp-In 293 T-Rex cells) expressing BirA*-LMOD1 and BirA*-LMOD2, were
801 generated as described by (Mackmull et al. 2017). The cells were selected using 15 µg/mL
802 Blasticidin (GibcoTM, R21001) and 100 µg/mL Zeocin™ (Thermo Fisher Scientific, R25001).
803 Once stable cell lines were generated, the cells were selected using 100 µg/mL Hygromycin B
804 (Thermo Fisher Scientific, 10687010) and 15 µg/mL Blasticidin (GibcoTM, R21001).
805 Stable HEK293T cell lines expressing fusion proteins containing BirA* were seeded in 150
806 mm dishes at the density of approximately 500K cells. To induce expression of BirA* fusion
807 proteins, cells were treated with 1 µg/mL tetracycline (Sigma Aldrich, 87128) for four days.
808 Biotin (50 µM) (Sigma Aldrich, B4501) was added to the cells 24 h prior to harvest to biotinylate
809 proximal proteins.

810 **Table 1: Primers for cloning**

Primer name	Sequence (5'-3')
Lmod1 sequencing primer (forward)	CTT GTG GCC GTT TAC GTC
Lmod1 sequencing primer (reverse)	CCCACTTGCTTGCTTTCATC
GFP sequencing primer (forward)	TAATACGACTCACTATAGGG
GFP sequencing primer (forward)	CGACTCACTATAGGGAGAGCGGC
pMSCV.puro sequencing primer (forward)	CGAGACCTCATCACCCAGG
T7 (forward)	TAATACGACTCACTATAGGG
pJet1.2 sequencing primer (forward)	CGACTCACTATAGGGAGAGCGGC
Lmod1_pcr_(forward)	CACCATGTCCAAAGTAGCTAAGTACCG
Lmod1.wSTOP (reverse)	TTATTGAAGTAGCTTGGGCACC
Lmod1.woSTOP (reverse)	TTGAAGTAGCTTGGGCACC
Lmod2.pcr (forward)	CACCATGTCTACGTTTGGCTACAGAAG
Lmod2.woSTOP (reverse)	TCTCAGAGCTTCGGGAACTTC
Lmod2.wSTOP (reverse)	TTATCTCAGAGCTTCGGGAACTTC

811

812 **Skeletal muscle cryostat sections and staining**

813 TA muscles were isolated and frozen sections (14 µm) were made using a Leica Cryostat CM
814 3050 (Meyer Instruments) at -21 °C and placed on glass slides. Sections were stored at -80
815 °C. For immunostaining, muscle cryosections were fixed with 4 % paraformaldehyde (v/v,
816 CP10.1, Roth, pH 7.4). for 7 min and then permeabilized with 0.1 M Glycine (1042011000,
817 VWR) in PBS, (pH 7.4) for 5 min and after one wash with PBS 0.5 %Triton-X was added (v/v,
818 3051.3, Roth) for 10 min. After another washing step with PBS sections were incubated for 20
819 min at 65 °C in pre-heated Citrate Antigen Retrieval buffer (10 mM Sodium citrate, 0.05 %
820 Tween 20, pH 6.0). Slides were re-equilibrated by washing 3x with PBS for 5 min and
821 incubated for 30 min using MOM blocking (1:40) and subsequently blocked in blocking solution
822 (5 % horse serum (v/v) in PBS) at RT. The sections were incubated in primary antibody Pax7
823 (Pax7, DSHB, Hybridoma mouse IgG1, undiluted), myogenin (DSHB, F5D, hybridoma cell
824 supernatant, undiluted), Lmod1 (Proteintech, 15117-1-AP, 1:500) and Laminin (LSBio, LS-
825 C96142, 1:500) overnight at 4 °C in a wet chamber. Sections were washed 3x with 0.1 %
826 Triton in PBS (pH 7.4) for 5 min and secondary antibodies anti-chicken IgG (Alexa Fluor® 488,
827 A-11039), anti-mouse IgG (Alexa Fluor® 546, A-21123, Thermo Fisher, 1:1000) and anti-
828 rabbit IgG (Alexa Fluor® 647, A-31573, Thermo Fisher, 1:1000), were applied for 1 h at RT.
829 Nuclei were stained with Hoechst (bisBenzimideH 33258, B2261 Sigma, 0.02 µg/µl in PBS,
830 1:5000) for 5 min. After washing sections 3x with 0.1 % Triton in PBS, sections were mounted
831 in Permafluor mountain medium (TA-006-FM, Thermo Fisher). Immunofluorescence
832 microscopy was performed with the Zeiss Axio Scan Z.1 using a Plan-Apochromat 20x/0.8
833 M27 Objective (Zeiss).

834 **Immunofluorescence staining of primary myoblasts**

835 Primary myoblasts from proliferation or differentiation assays were fixed with 2 %
836 formaldehyde (v/v in PBS, CP10.1, Roth) for 5 min at RT, washed twice with PBS for 5 min
837 and were permeabilized with permeabilization solution (0.1 % Triton-X-100 (v/v, 3051.3, Roth),
838 0.1 M Glycine (1042011000, VWR) in PBS) for 5 min at RT. Cells were incubated for 1 h in
839 blocking solution (5 % horse serum, v/v, 26050-088, Thermo Fisher) in PBS at RT. Incubation
840 with primary antibodies was carried out in 5 % horse serum in PBS overnight at 4 °C.
841 Subsequently, the cells were washed three times with PBS for 5 min and incubated with the
842 secondary antibodies in blocking solution for 1 h at RT in the dark. Next, the cells were washed
843 once with PBS for 5 min, stained with Hoechst (bisBenzimide H 33258, B2261 Sigma, 1:5000
844 in PBS) at RT for 5 min and washed twice with PBS for 5 min. The cells were stored at 4 °C
845 in PBS in the dark until they were analyzed. For location stainings, the removable chamber
846 was detached, and cells were mounted in permafluor mounting medium (TA-006-FM, Thermo
847 Fisher) and coverslips (631-1574, VWR). The cells were then analyzed using an Axio
848 Observer microscope (Carl Zeiss) or with an Axio Imager (Z2 using a Plan-Apochromat 63 x /
849 0.8 M27 Objective) and analyzed with Zen 2 Blue Edition software (Carl Zeiss Microscopy
850 GmbH).

851 Primary antibodies used for immunofluorescence analysis (Table 3): Hybridoma mouse IgG1
852 myogenin (DSHB, F5D, hybridoma cell supernatant, undiluted), Hybridoma mouse IgG1
853 devMHC (DSHB, MF20, hybridoma cell supernatant, undiluted), anti-ki67 (ab15580, rabbit IgG
854 1:500), Lmod1 (Proteintech, 15117-1-A, rabbit, IgG, 1:500) and Sirt1 (Proteintech, 60303-1-
855 Ig, mouse, IgG2b, 1:400). Secondary antibodies: anti-mouse IgG2b (Alexa Fluor® 488, A-
856 21141, Thermo Fisher, 1:1000), anti-rabbit IgG (Alexa Fluor® 546, A10040, Thermo Fisher,
857 1:1000), anti-mouse IgG (Alexa Fluor® 546, A-21123, Thermo Fisher, 1:1000)

858

859 **Immunofluorescence staining of HEK293T cells**

860 The cells were washed 3x with 1 x PBS and fixed in 4 % formaldehyde (v/v) in PBS for 10
861 minutes at room temperature. After that, cells were washed again 3x with 1 x PBS and
862 permeabilized using a permeabilization buffer (0.7 % Triton X-100 in 1 x PBS) for 15 minutes
863 at room temperature, followed by two washing steps with PBS for 5 minutes each. The
864 samples were incubated with a blocking solution (10 % (w/v) BSA, 10 % (v/v) Triton X-100, 5
865 % (v/v) goat serum) for 1h at room temperature. The coverslips were incubated with primary
866 antibody anti-FLAG (Sigma-Aldrich, mouse, F1804, 1:500) at 4 °C overnight. After washing 3x
867 with PBS, the secondary fluorescence-labeled antibody anti-mouse IgG (Alexa Fluor® 488, A-
868 21121, Thermo Fisher, 1:1000) in blocking solution and anti-biotin (Streptavidin AlexaFuor®
869 568, S11226, Thermo Fisher, 1:2000) in blocking solution were incubated for 1 h at RT. After
870 washing once with PBS nuclei were stained with Hoechst (bisBenzimideH 33258, B2261

871 Sigma, 0.02 µg/µl in PBS, 1:5000) at RT for 5 minutes. and were finally washed twice for 5
872 minutes with PBS. Finally, the samples were washed twice with PBS for 5 minutes, and cells
873 were mounted in Permafluor mounting medium (TA-006-FM, Thermo Fisher) and coverslips
874 (631-1574, VWR). Immunofluorescence microscopy was performed with an Axio Imager (Z2
875 using a Plan-Apochromat 63 x / 0.8 M27 Objective) and analyzed with Zen 2 Blue Edition
876 software (Carl Zeiss Microscopy GmbH).
877
878 **Proximity ligation assay**
879 Primary myoblasts were cultured in a collagen-coated removable 12-well chamber (81201,
880 Ibid) and fixed in 2 % PFA for 5 minutes at RT. Subsequently, the proximity ligation assay
881 (PLA) (#DUO92008, Sigma-Aldrich) was performed according to the manufacturer's protocol.
882 Anti-Sirt1 antibodies and anti-Lmod1 antibodies were incubated overnight at 4 °C.
883 Immunofluorescent pictures were taken with an Axio Imager (Z2 using a Plan-Apochromat 63x
884 / 0.8 M27 Objective) and analyzed with Zen 2 Blue Edition software (Carl Zeiss Microscopy
885 GmbH).
886
887 **Harvesting and lysis of cells for immunoblotting**
888 To harvest the cultured cells from proliferation or differentiation assay, the medium was
889 removed and the cells were washed with PBS at RT. Then, 50 µl RIPA buffer (150 mM Sodium
890 Chloride (P029.2, Roth), 1 % Triton X-100 (v/v, 3051.3, Roth), 0.5 % Sodium Deoxycholate
891 (89904, Thermo Fisher), 0.1 % SDS (w/v, 75746-250G, Sigma), 50 mM Tris (4855.2, Roth),
892 pH8) was added to each well of the 24 well plate. The cells were carefully scraped off the plate
893 by using a cell scraper. Cells were incubated on ice for 20 min and mixed by vortexing every
894 5 min. Cell lysis was completed by sonication using Diagenode's Bioruptor® Plus 10x for 1
895 min (1 min 'on', 30 sec 'off').
896 Primary antibodies used for immunoblotting analysis: anti-BirA (Novus Biologicals, 5B11c3-3,
897 1:500), anti-GFP (Santa Cruz, sc-9996, 1:1000), anti-mouse (Agilent Dako, P0448, 1:1500)
898 anti-Lmod1 (Proteintech, 15117-1-AP, 1:500), anti-Lmod2 (Atlas Antibodies, HPA051039,
899 1:500), anti-Sirt1 (Proteintech, 60303-1-Ig, 1:1000), anti-Aldoa (Proteintech, 67453-1-Ig,
900 1:20.000), anti-H4 (Cell Signaling, #2935, 1:1000), anti-Gapdh (SantaCruz, sc-365062,
901 1:200). Secondary antibodies: anti-rabbit (Agilent Dako, P0447, 1:2000), anti-mouse (Agilent
902 Dako, P0448, 1:1500).

903 **Table 3: Antibody-List**

Antibody name	Source	Product number
Monoclonal rat IgG2a Sca1-FITC	eBioscience	11-5981-85RRID:AB_465334
Monoclonal rat IgG2a Sca1-PE (Ly-6A/E-PE)	BDBioscience	553108RRID:AB_394629
Hybridoma mouse IgG1 Pax7	DSHB	Pax7RRID:AB_528428
Polyclonal rabbit IgG Lmod1	Proteintech	15117-1-AP
Polyclonal human IgG Lmod2	Atlas Antibodies	HPA051039
Polyclonal chicken IgG Laminin	LSBio	LS-C96142
Hybridoma mouse IgG1 myogenin	DSHB	F5D
Hybridoma mouse IgG1 devMHC	DSHB	MF20
Polyclonal rabbit IgG Ki-67	Abcam	ab15580
Monoclonal mouse IgG2b Sirt1	Proteintech	60303-1-Ig
bisBenzimideH 33258 (Hoechst)	Sigma-Aldrich	B2261
Monoclonal mouse M2 Flag	Sigma-Aldrich	F1804
Monoclonal mouse IgG GFP	Santa Cruz	Sc-9996
Monoclonal mouse IgG BirA	Novus Biologicals	5B11c3-3
Monoclonal mouse IgG1 Gapdh	SantaCruz	sc-365062
Monoclonal mouse IgG H4 (L64C1)	Cell Signaling	#2935
Monoclonal mouse IgG Aldoa	Proteintech	67453-1-Ig
anti-mouse IgG Alexa Fluor® 488	Thermo Fisher	A-21121
anti-mouse IgG Alexa Fluor® 546	Thermo Fisher	A-21123
anti-mouse IgG2b Alexa Fluor® 488	Thermo Fisher	A-21141
anti-mouse IgG2b Alexa Fluor® 488	Thermo Fisher	A-21242
anti-rabbit IgG Alexa Fluor® 488	Thermo Fisher	A-21206
anti-rabbit IgG Alexa Fluor® 546	Thermo Fisher	A10040
anti-rabbit IgG Alexa Fluor® 647	Thermo Fisher	A-31573
anti-chicken IgG Alexa Fluor® 488	Thermo Fisher	A-11039
Anti-Streptavidin Alexa Fluor ® 568	Thermo Fisher	S11226
Anti-Mouse Immunoglobulins/HRP	Agilent Dako	P0448
Anti-Rabbit Immunoglobulins/HRP	Agilent Dako	P0447

904

905 **Protein quantification assays**

906 The EZQ™ Protein Quantitation Kit (R33200, Thermo Fisher) and the Invitrogen™ Qubit™ 3
907 Fluorometer (15387293, Invitrogen), together with Qubit™ assay tubes (Q32856, Invitrogen),
908 were used to quantify protein samples according to the manufacturer's protocols. The TECAN
909 microplate reader (1405005206, Tecan INFINITE M1000 PRO, excitation 485 nm, emission
910 580 nm) was used to analyze the EZQ assay.

911

912 **GFP Trap**

913 For the generation of cell lines transiently expressing Sirt1 fused to GFP or GFP control,
914 plasmids were generated using Gateway Technology (Invitrogen). Four 10 cm dishes of
915 HEK293T cells (3 million cells/dish) were used for each candidate, and prior to transfection,
916 the medium was replaced with a transfection medium (DMEM with 1 % FBS, without
917 antibiotics). Each plate was transfected with 5 µg plasmid DNA and 15 µg Polyethylenimine
918 (PEI 25K™, Polysciences, 23966-100), both previously prepared in OptiMEM (Gibco,
919 11520386). The transfection medium was changed to 5 mL DMEM with 10 % FBS and 1 %
920 Pen-Strep 6 h post-transfection. Additionally, 5 µl (1 mg/mL) of Tetracycline was to the media
921 and cells were incubated for 48 h at 3.5 % CO2, 37 °C. Subsequently, cells were harvested
922 by trypsinization, and 20 million cells per pellet were collected for GFP-Trap pull-down. Each
923 pellet was lysed in 200 µl of lysis buffer (20 mM Tris pH 7.5, 150 mM NaCl, 1 mM EDTA, 0.3
924 % Triton, 10 % Glycerol) containing protease and phosphatase inhibitors. Tubes were placed
925 on ice for 30 min with vortexing every 10 min, followed by brief sonication in a Bioruptor Plus
926 for 5 cycles (30 sec on/30 sec off) at the highest setting and afterwards centrifuged at 20000x
927 *g*, for 10 min at 4 °C. Lysate-supernatants were transferred to a pre-cooled tube and to each
928 of them 300 µl dilution buffer (10 mM Tris pH 7.5, 150 mM NaCl, 0.5 mM EDTA), was added.
929 25 µl of GFP Trap beads (ChromoTek GFP-Trap® Agarose, Proteintech, gta) were
930 equilibrated in 0.5 mL of ice-cold dilution buffer and were spun down at 100x *g* for 5-10 sec at
931 4 °C. Beads were washed two more times with 500 µl dilution buffer. Cell lysates were added
932 to equilibrated GFP Trap beads and incubated for 1 h at 4 °C with constant mixing. Tubes
933 were spun at 100x *g* for 5-10 sec at 4 °C. GFP Trap beads were washed with 500 µl ice-cold
934 dilution buffer, followed by two washes with wash buffer (10 mM Tris pH 7.5, 150 mM NaCl,
935 0.05 % P40 Substitute, 0.5 mM EDTA). To elute proteins, 2 x 30 µl of 2x SDS-sample buffer
936 (120 mM Tris pH 6.8, 20 % glycerol, 4 % SDS, 0.04 % bromophenol blue) was added to the
937 GFP Trap beads and boiled for 5 min at 95 °C. Subsequently, the beads were collected by
938 centrifugation at 2500x *g* for 2 min and supernatant was collected to perform an SDS-PAGE.

939 **Nuclear cytoplasmic fractionation experiment**

940 Nuclear cytoplasmic fractionation was performed seeding 3 x 10^6 primary myoblasts. Prior cell
941 harvest, cells were washed twice with 10 mL of PBS at RT to remove any residual media.
942 Then, they were trypsinized with 0.25 % Trypsin and resuspended in 8 mL of myoblasts growth
943 medium. After centrifuging at 500x *g* for 5 minutes, the supernatant was discarded, and the
944 cells were resuspended in 5 mL of ice-cold PBS. At this stage, the total number of cells was
945 counted. For hypotonic lysis, the cells were spun at 4 °C and 500x *g*. The resulting pellet was
946 resuspended in 500-700 µl of Buffer A (10 mM Tris pH 7.5) containing protease inhibitor. The
947 cells were incubated on ice for 20-30 minutes, and their swelling was monitored. Then, they
948 were lysed by passing them through a 27G needle 15-30 times. The process was stopped
949 when 70-80 % of the cells were lysed to prevent nuclei breakdown. Nuclei were manually
950 counted to calculate the ratio of nuclei to total cells. The lysed cells were centrifuged at 1000x
951 *g* at 4 °C to separate nuclei, and the supernatant was collected as the cytoplasmic fraction.
952 The pellet of nuclei was resuspended in 60-100 µl of Buffer B (0.25 M sucrose, 50 mM Tris
953 pH 7.5, 25 mM Kcl, 5 mM MgCl2, 2 mM DTT) with protease inhibitor and the nuclei were
954 manually counted using a hemocytometer.

955

956 **RNA isolation**

957 RNA isolation was performed with TriFast (Peqlab) according to the manufacturer's protocol.
958 Primary myoblasts were either directly harvested into TriFast or cell pellets were resuspended
959 and lysed by pipetting.

960

961 **cDNA synthesis**

962 cDNA was synthesized by reverse transcription using 600 ng of isolated RNA. The GoScript™
963 Reverse Transcriptase kit (A5001, Promega) was used according to the manufacturer's
964 protocol. Finally, the cDNA was diluted 1:10 and stored at -20 °C until further analysis.

965

966 **qRT-PCR**

967 Quantitative real-time PCR was performed on a CFX384 Touch Real-Time PCR Detection
968 System (Biorad). One qRT-PCR reaction mix consists of 3 µl cDNA, 5 µl iQ SYBR™ Green
969 Supermix (1708882, Biorad), 1 µl sterile ddH2O and 0.5 µl of 10 µM forward and reverse
970 primer (Metabion, ordered as 100 µM stock in sterile ddH2O, sequences listed in Table 2).
971 Technical triplicates were performed for each sample. For triplicates having a Cq-SEM
972 (calculated by Bio-Rad CFX Maestro 1.1) higher than 0.4, the replicate with the largest
973 difference was excluded. The obtained Ct-values of target genes and housekeeping genes
974 were used to calculate relative expression according to the $2^{-\Delta\Delta Ct}$ formula (Pfaffl 2001).

975 **Table 2: Primers for qRT-PCR**

Primer name	Sequence (5'-3')
GAPDH (forward)	ATGCCAGTGAGCTTCCCGTC
GAPDH (reverse)	CATCACCATCTTCCAGGAGC
Lmod1 (forward)	AAAAGACAGGAGTGTCAAGAAC
Lmod1 (reverse)	CCCCAGAACCTATGCCCTC
Lmod2 (forward)	ACCTTATCCCGATTTGCTGAAG
Lmod2 (reverse)	ACCTTGAGCATGTCTGCAATG
MyoD (forward)	CTACAGTGGCGACTCAGAT
MyoD (reverse)	CACTGTAGTAGGCGGTGTC
Myogenin (forward)	CAGTACATTGAGCGCCTAC
Myogenin (reverse)	AAGGCAACAGACATATCCTC
Pax7 (forward)	TCTTACTGCCCACCCACCTA
Pax7 (reverse)	CACGTTTTTGGCCAGGTAAT
Sirt1 (forward)	TGATTGGCACCGATCCTCG
Sirt1 (reverse)	CCACAGCGTCATATCATCCAG
18S (forward)	CCATCCAATCGGTAGTAGCG
18S (reverse)	GTAACCCGTTGAACCCCATT

976

977 **RNA Sequencing**

978 Primary myoblasts were seeded and pre-treated with siRNA against Lmod1 and Sirt1 for two
979 days under proliferating conditions. A second transfection with siLmod1 and siSirt1 was
980 performed simultaneously with the induction of differentiation. After one day of differentiation,
981 the cells were collected in TriFast and RNA was isolated using the procedure described above.
982 The concentration and integrity of the isolated RNA was determined using Qubit 3.0
983 Fluorometer (Thermo Fisher), Bioanalyzer 2100, and Tapestation RNA (Agilent). To prepare
984 the poly-A library, TruSeq RNA Library Prep Kit v2 (Illumina, RS-122-2001) was used
985 according to the manufacturer's protocol. The process started with the enrichment of poly-A-
986 containing mRNA using magnetic beads, followed by first-strand synthesis of cDNA using
987 SuperScript III Reverse Transcriptase (Thermo Fisher). The second strand synthesis was
988 performed using the second strand master mix (TruSeq RNA Library Prep Kit v2 (Illumina)),
989 and the DNA was cleaned up using Agencourt AMPure XP Beads (Beckman Coulter,
990 A63881). After end repair and dA-tailing, adaptors were ligated, and the library was further
991 enriched using the PCR Master Mix (TruSeq RNA Library Prep Kit v2 (Illumina)). The
992 concentration and quality of the library were determined using Qubit 3.0 Fluorometer (Thermo
993 Fisher), Bioanalyzer 2100, and Tapestation DNA (Agilent). Finally, the libraries were pooled
994 and RNA-Seq and data analysis was performed by Azenta US using Illumina NovaSeq (USA;
995 www.GENEWIZ.com).

996 **Whole proteome analysis**

997 For proteomics analysis of myoblasts or Lmod1 overexpression cell lines, samples were
998 sonicated (Bioruptor Plus, Diagenode, Belgium) for 10 cycles (60 sec ON/30 sec OFF) at high
999 setting, at 20 °C, followed by boiling at 95 °C for 5 min. Reduction with 10 mM Dithiothreitol
1000 (DTT) (6908.3, Roth) for 15 min was followed by alkylation with iodoacetamide (IAA, final
1001 concentration 15 mM) for 30 min at room temperature in the dark. Protein amounts were
1002 estimated following an SDS-PAGE gel of 10 µL of each sample against an in-house cell lysate
1003 of known quantity. 30 µg of each sample was used for digestion. Proteins were precipitated
1004 overnight at -20 °C after addition of 4x volume of ice-cold acetone. The following day, the
1005 samples were centrifuged at 20800x *g* for 30 min at 4 °C and the supernatant was carefully
1006 removed. Pellets were washed twice with 300 µL ice-cold 80 % (v/v) acetone in water and
1007 then centrifuged at 20800x *g* at 4 °C for 10 min. After removing the acetone, pellets were air-
1008 dried before addition of 25 µL of digestion buffer (1M Guanidine, 100 mM HEPES, pH 8).
1009 Samples were resuspended with sonication as explained above, then LysC (Wako) was added
1010 at 1:100 (w/w) enzyme:protein ratio and digestion proceeded for 4 h at 37 °C under shaking
1011 (1000 rpm for 1 h, then 650 rpm). Samples were then diluted 1:1 with MilliQ water and trypsin
1012 (Promega) added at at 1:100 (w/w) enzyme:protein ratio. Samples were further digested
1013 overnight at 37 °C under shaking (650 rpm). The day after, digests were acidified by the
1014 addition of TFA to a final concentration of 10 % (v/v), heated at 37 °C and then desalted with
1015 Waters Oasis® HLB µElution Plate 30 µm (Waters Corporation, MA, USA) under a soft
1016 vacuum following the manufacturer instruction. Briefly, the columns were conditioned with
1017 3x100 µL solvent B (80 % (v/v) acetonitrile; 0.05 % (v/v) formic acid) and equilibrated with
1018 3x100 µL solvent A (0.05 % (v/v) formic acid in Milli-Q water). The samples were loaded,
1019 washed 3 times with 100 µL solvent A, and then eluted into 0.2 mL PCR tubes with 50 µL
1020 solvent B. The eluates were dried down using a speed vacuum centrifuge (Eppendorf
1021 Concentrator Plus, Eppendorf AG, Germany). Dried samples were stored at -20 °C until
1022 analysis.

1023

1024 **Enrichment and digestion of biotinylated proteins (BioID)**

1025 The protocol was used as described in Bartolome et al (Bartolome et al. 2023). In short, pellets
1026 corresponding to 20 Mio cells were resuspended in 4.75 mL lysis buffer (50 mM Tris pH 7.5;
1027 150 mM NaCl; 1 mM EDTA; 1mM EGTA; 1 % (v/v) Triton X-100; 1 mg/ml aprotinin; 0.5 mg/ml
1028 leupeptin; 250 U turbonuclease; 0.1 % (w/v) SDS) and incubated for 1 h at 4 °C. Streptavidin
1029 Sepharose High Performance (GE Healthcare) was acetylated by the addition of 10 mM sulfo-
1030 NHS acetate (Thermo Fisher Scientific) for 30 min twice and then equilibrated in lysis buffer.
1031 For each lysate 80 µl of equilibrated beads were used. Upon loading, beads were washed 5
1032 times with 600 µl 50 mM AmBic. On-bead digest was performed with 200 µl LysC (5 ng/µl) at

1033 37 °C overnight. First elution step was achieved using two times 150 µl of 50 mM AmBic. After
1034 pooling both fractions, peptides were further digested off-beads by adding 1 µg trypsin and
1035 incubating at 37 °C for 3 h. Biotinylated peptides were eluted in a second elution step using
1036 two times 150 µl 20 % TFA (Biosolve) in acetonitrile (Biosolve). Both fractions were pooled
1037 and neutralized to pH 8.0 by adding 50 µl 200 mM HEPES and sodium hydroxide as
1038 necessary. Peptides were digested further off-beads by adding 1 µg trypsin at 37 °C for 3 h.
1039 Digested peptides from the two elution steps were desalted using Waters Oasis® HLB
1040 µElution Plate 30 µm (Waters) according to the manufacturer's instructions.
1041
1042 **LC-MS/MS analysis**
1043 Peptides were reconstituted in 10 µl reconstitution buffer at a concentration of 1 µg/µl, 0.5 µl
1044 of the HRM kit (Ki-3002-1, Biognosys) was added in a dilution recommended by the
1045 manufacturer and 1 µl were injected for measurement. Peptides were separated using the
1046 UltiMate 3000 UPLC system (Thermo Fisher Scientific, for myoblasts) or nanoAcquity UPLC
1047 system (Waters, for BioID and Lmod1 overexpressing cell lines) fitted with trapping
1048 (nanoAcquity Symmetry C18, 5µm, 180 µm x 20 mm) and an analytical column (nanoAcquity
1049 BEH C18, 1.7µm, 75µm x 250mm). The outlet of the analytical column was coupled directly
1050 to Q-exactive HF (Thermo Fisher Scientific, for myoblasts) or Orbitrap Exploris 480 (Thermo
1051 Fisher Scientific, for BioID and Lmod1 overexpressing cell lines) using the Proxeon nanospray
1052 source. For myoblast experiment, solvent A was water, 0.1 % FA and solvent B was 80 %
1053 (v/v) acetonitrile, 0.08 % FA. Peptides were eluted via a non-linear gradient from 1 % to 62.5
1054 % B in 131 min. Total runtime was 150 min, including clean-up and column re-equilibration.
1055 The peptides were introduced into the mass spectrometer via a Pico-Tip Emitter 360 µm OD
1056 x 20 µm ID; 10 µm tip (New Objective) and a spray voltage of 2.2 kV was applied. The RF ion
1057 funnel was set to 60 %.
1058 Data Dependent Acquisition (DDA) settings were as follows: Full scan MS spectra with mass
1059 range 350-1650m/z were acquired in the Orbitrap with a resolution of 60,000 FWHM. The
1060 filling time was set at a maximum of 20ms with an AGC target of $3x10^6$ ions. A Top15 method
1061 was employed to select precursor ions from the full scan MS for fragmentation (minimum AGC
1062 target of $1x\ 10^3$ ions, normalized collision energy of 27 %), quadrupole isolation (1.6 m/z) and
1063 measurement in the Orbitrap (resolution 15,000 FWHM, fixed first mass 120 m/z). The
1064 fragmentation was performed after the accumulation of $2x10^5$ ions or after filling time of 25ms
1065 for each precursor ion (whichever occurred first). Only multiply charged (2+ -7+) precursor
1066 ions were selected for MS/MS. Dynamic exclusion was employed with a maximum retention
1067 period of 20s. Isotopes were excluded.
1068 For Data Independent Acquisition (DIA), 1 µg of reconstituted peptides were loaded using the
1069 same setup and LC conditions used for DDA. MS conditions were modified as follows: Full

1070 scan MS spectra with mass range 350-1650 m/z were acquired in profile mode in the Orbitrap
1071 with resolution of 120,000 FWHM. The filling time was set at a maximum of 60 ms with an
1072 AGC target of $3x10^6$ ions. DIA scans were acquired with 40 mass window segments of differing
1073 widths across the MS1 mass range. The default charge state was set to 3+. HCD
1074 fragmentation (stepped normalized collision energy; 25.5, 27, 30 %) was applied and MS/MS
1075 spectra were acquired with a resolution of 30,000 FWHM with a fixed first mass of 200 m/z
1076 after accumulation of $3x\ 10^6$ ions or after a filling time of 35ms (whichever occurred first). Data
1077 was acquired in profile mode. For data acquisition and processing Tune version 2.9 Q-
1078 Exactive HF
1079 For BioID project experiment and, solvent A was water, 0.1 % FA and solvent B was 80 %
1080 (v/v) acetonitrile, 0.08 % FA. Peptides were eluted via a non-linear gradient from 3 % to 40 %
1081 B in 90 min. Total runtime was 115 min, including clean-up and column re-equilibration. The
1082 peptides were introduced into the mass spectrometer via a Pico-Tip Emitter 360 µm OD x 20
1083 µm ID; 10 µm tip (New Objective) and a spray voltage of 2.2 kV was applied. The RF ion funnel
1084 was set to 30 %. For Data Independent Acquisition (DIA), MS conditions were modified as
1085 follows: Full scan MS spectra with mass range 350-1650 m/z were acquired in profile mode in
1086 the Orbitrap with resolution of 120,000 FWHM. The filling time was set at a maximum of 60
1087 ms with an AGC target of $3x10^6$ ions (300 %). DIA scans were acquired with 34 mass window
1088 segments of differing widths across the MS1 mass range. The default charge state was set to
1089 2+. HCD fragmentation (stepped normalized collision energy; 25.5, 27, 30 %) was applied and
1090 MS/MS spectra were acquired with a resolution of 30,000 FWHM with a fixed first mass of 200
1091 m/z after accumulation of $3x\ 10^6$ ions (3000 %) or after a filling time of 40ms (whichever
1092 occurred first). Data was acquired in profile mode. For data acquisition and processing Tune
1093 3.1.
1094 For Lmod1 overexpressing cell line experiment, solvent A was water, 0.1 % FA and solvent B
1095 was acetonitrile, 0.1 % FA. Peptides were eluted via a non-linear gradient from 3 % to 40 % B
1096 in 120 min. Total runtime was 145 min, including clean-up and column re-equilibration. The
1097 peptides were introduced into the mass spectrometer via a Pico-Tip Emitter 360 µm OD x 20
1098 µm ID; 10 µm tip (New Objective) and a spray voltage of 2.2 kV was applied. The RF ion funnel
1099 was set to 30 %. For Data Independent Acquisition (DIA), 1 µg of reconstituted peptides were
1100 loaded using the same setup and LC conditions used for DDA. MS conditions were modified
1101 as follows: Full scan MS spectra with mass range 350-1650 m/z were acquired in profile mode
1102 in the Orbitrap with resolution of 120,000 FWHM. The filling time was set at a maximum of 60
1103 ms with an AGC target of $3x10^6$ ions. DIA scans were acquired with 40 mass window segments
1104 of differing widths across the MS1 mass range. The default charge state was set to 3+. HCD
1105 fragmentation (stepped normalized collision energy; 25.5, 27, 30 %) was applied and MS/MS
1106 spectra were acquired with a resolution of 30,000 FWHM with a fixed first mass of 200 m/z

1107 after accumulation of 3x 10^6 ions or after a filling time of 35 ms (whichever occurred first). Data
1108 was acquired in profile mode. For data acquisition and processing Tune 2.0.
1109
1110 **Proteomics data analysis**
1111 For myoblasts DIA search against a library was performed. Acquired data were processed
1112 using Spectronaut Professional v13 (Biognosys AG). For library creation, the DDA and DIA
1113 raw files were searched with Pulsar (Biognosys AG) against the mouse UniProt database (*Mus*
1114 *musculus,* v. 160106, 16,747 entries) with a list of common contaminants (247 entries)
1115 Swissprot database appended, using default settings. For library generation, default BGS
1116 factory settings were used.
1117 DIA data were then uploaded and searched against this spectral library using Spectronaut
1118 Professional (v.10 and v.13 Biognosys) and default settings. Relative quantification was
1119 performed in Spectronaut for each pairwise comparison using a two-sided t-test performed at
1120 the precursor level followed by multiple testing correction and default settings, except: Major
1121 Group Quantity = median peptide quantity; Major Group Top N = OFF; Minor Group Quantity
1122 = median precursor quantity; Minor Group Top N = OFF; Data Filtering = Q value sparse;
1123 Normalization Strategy = Local normalization; Row Selection = Q value complete.
1124 For Lmod1 overexpression cell lines, DIA raw data were analyzed using the directDIA pipeline
1125 in Spectronaut v.14 (Biognosysis, Switzerland) with BGS settings besides the following
1126 parameters: Protein LFQ method= QUANT 2.0, Proteotypicity Filter = Only protein group
1127 specific, Major Group Quantity = Median peptide quantity, Minor Group Quantity = Median
1128 precursor quantity, Data Filtering = Qvalue, Normalizing strategy = Local Normalization. The
1129 data were searched against an in-house database (*Mus Musculus*, 16,747 entries) and a
1130 contaminants (247 entries) Swissprot database. The data were searched with the following
1131 variable modifications: Oxidation (M) and Acetyl (Protein N-term). A maximum of 2 missed
1132 cleavages for trypsin and 5 variable modifications were allowed. The identifications were
1133 filtered to satisfy FDR of 1 % on peptide and protein level. Relative quantification was
1134 performed in Spectronaut for each paired comparison using the replicate samples from each
1135 condition. The data (candidate table) and data reports (protein quantities) were then exported,
1136 and further data analyses and visualization were performed with Rstudio using in-house
1137 pipelines and scripts.
1138 BioID DIA raw data were analyzed using the directDIA pipeline in Spectronaut with v.15. The
1139 data were searched against a specific species (*Homo sapiens,* v. 160112, 20,375 entries) and
1140 a contaminants (247 entries) Swissprot database. The data were searched with the following
1141 modifications: Oxidation (M), Acetyl (Protein N-term) and Biotin_K. A maximum of 2 missed
1142 cleavages for trypsin and 5 variable modifications were allowed. The identifications were
1143 filtered to satisfy FDR of 1 % on peptide and protein level. Relative quantification was

1144 performed in Spectronaut using LFQ QUANT 2.0 method with Global Normalization, precursor
1145 filtering percentile using fraction 0.2 and global imputation. The data (candidate table) and
1146 data reports (protein quantities) were then exported, and further data analyses and
1147 visualization were performed with Rstudio using in-house pipelines and scripts.
1148
1149 **Clustering and gene set enrichment analysis**
1150 Proteomics data for the myoblast differentiation time course were filtered for protein groups
1151 quantified by at least two unique (proteotypic) peptides. All the differentiation time points
1152 (1d:5d) were compared to undifferentiated myoblast (0d) and protein groups that showed an
1153 absolute AVG Log2 Ratio > 0.58 and Q value < 0.25 at any time point were selected for
1154 clustering analysis. Determination of an optimal number of clusters, clustering, and enrichment
1155 analysis for each cluster was performed with ClueR (Yang et al. 2015) using the AVG Log2
1156 Ratios to 0d as input.
1157 A gene set was created to analyze the LMOD1 overexpression cell line using all the protein
1158 groups differentially abundant in 1d vs. 0d myoblast differentiation time course (AVG Log2
1159 Ratio > 0.58 and Q value < 0.05). This gene set was used as input for a gene set enrichment
1160 analysis based on AVG Log2 Ratios from the comparison of LMOD1 OE vs. GFP OE
1161 performed with WebGestalt (Liao et al. 2019).
1162
1163 **Statistical analysis**
1164 Mouse and cell line experiments were performed at least in biological triplicates, and numbers
1165 are indicated in the figure legends. The results are shown as the mean ± SEM unless indicated
1166 otherwise in the figure legends. Statistical significance was calculated using the GraphPad
1167 Prism software using the statistical test indicated in the figure legends, with *: p 0.05, **: p 0.01,
1168 ***: p 0.001, ****: p 0.0001 and ns (not significant) or nd (not detectable). RNA-seq approaches
1169 were conducted in biological replicates (n = 5) using primary myoblasts isolated from individual
1170 mice per experimental group, and statistical analysis is described in the respective section.

Data availability

The mass spectrometry proteomics data have been deposited to the MassIVE (https://massive.ucsd.edu) repository with the following dataset identifier:

Proteomic dataset: MSV000093379
Username: MSV000093379_reviewer
Password: ES_Lmod1

RNA-Seq data have been deposited on Gene Expression Omnibus (GEO) international public repository at: GSE254443
Password: epkbcyyinjmxzmd

1183 **REFERENCES**

1184 Abdel Khalek, Waed, Fabienne Cortade, Vincent Ollendorff, Laure Lapasset, Lionel
1185 Tintignac, Béatrice Chabi, and Chantal Wrutniak-Cabello. 2014. "SIRT3, a Mitochondrial
1186 NAD^+-Dependent Deacetylase, Is Involved in the Regulation of Myoblast
1187 Differentiation." *PloS One* 9 (12): e114388.
1188 Abmayr, Susan M., and Grace K. Pavlath. 2012. "Myoblast Fusion: Lessons from Flies and
1189 Mice." *Development* 139 (4): 641–56.
1190 Armand, Anne-Sophie, Iman Laziz, and Christophe Chanoine. 2006. "FGF6 in Myogenesis."
1191 *Biochimica et Biophysica Acta* 1763 (8): 773–78.
1192 Baghdadi, Meryem B., David Castel, Léo Machado, So-Ichiro Fukada, David E. Birk,
1193 Frederic Relaix, Shahragim Tajbakhsh, and Philippos Mourikis. 2018. "Reciprocal
1194 Signalling by Notch-Collagen V-CALCR Retains Muscle Stem Cells in Their Niche."
1195 *Nature* 557 (7707): 714–18.
1196 Baghdadi, Meryem B., Joao Firmino, Kartik Soni, Brendan Evano, Daniela Di Girolamo,
1197 Philippos Mourikis, David Castel, and Shahragim Tajbakhsh. 2018. "Notch-Induced
1198 miR-708 Antagonizes Satellite Cell Migration and Maintains Quiescence." *Cell Stem*
1199 *Cell* 23 (6): 859–68.e5.
1200 Bai, Wenlong, and Xiaohong Zhang. 2016. "Nucleus or Cytoplasm? The Mysterious Case of
1201 SIRT1's Subcellular Localization." *Cell Cycle* 15 (24): 3337–38.
1202 Bartolome, Aleksandar, Julia C. Heiby, Domenico Di Fraia, Ivonne Heinze, Hannah Knaudt,
1203 Ellen Späth, Omid Omrani, et al. 2023. "ProteasomeID: Quantitative Mapping of
1204 Proteasome Interactomes and Substrates for in Vitro and in Vivo Studies." *bioRxiv*.
1205 https://doi.org/10.1101/2022.08.09.503299.
1206 Bentzinger, C. Florian, Yu Xin Wang, Nicolas A. Dumont, and Michael A. Rudnicki. 2013.
1207 "Cellular Dynamics in the Muscle Satellite Cell Niche." *EMBO Reports* 14 (12): 1062–72.
1208 Bentzinger, C. Florian, Yu Xin Wang, Julia von Maltzahn, Vahab D. Soleimani, Hang Yin,
1209 and Michael A. Rudnicki. 2013. "Fibronectin Regulates Wnt7a Signaling and Satellite
1210 Cell Expansion." *Cell Stem Cell* 12 (1): 75–87.
1211 Boczkowska, Malgorzata, Grzegorz Rebowski, Elena Kremneva, Pekka Lappalainen, and
1212 Roberto Dominguez. 2015. "How Leiomodin and Tropomodulin Use a Common Fold for
1213 Different Actin Assembly Functions." *Nature Communications* 6 (1): 1–12.
1214 Brack, Andrew S., Heidi Bildsoe, and Simon M. Hughes. 2005. "Evidence That Satellite Cell
1215 Decrement Contributes to Preferential Decline in Nuclear Number from Large Fibres
1216 during Murine Age-Related Muscle Atrophy." *Journal of Cell Science* 118 (Pt 20): 4813–
1217 21.
1218 Broussy, Sylvain, Hanna Laaroussi, and Michel Vidal. 2020. "Biochemical Mechanism and
1219 Biological Effects of the Inhibition of Silent Information Regulator 1 (SIRT1) by EX-527
1220 (SEN0014196 or Selisistat)." *Journal of Enzyme Inhibition and Medicinal Chemistry* 35
1221 (1): 1124–36.
1222 Budai, Zsofia, Laszlo Balogh, and Zsolt Sarang. 2018. "Altered Gene Expression of Muscle
1223 Satellite Cells Contributes to Agerelated Sarcopenia in Mice." *Current Aging Science* 11
1224 (3): 165–72.
1225 Chakkalakal, Joe V., Kieran M. Jones, M. Albert Basson, and Andrew S. Brack. 2012. "The
1226 Aged Niche Disrupts Muscle Stem Cell Quiescence." *Nature* 490 (7420): 355–60.
1227 Chang, Natasha C., and Michael A. Rudnicki. 2014. "Satellite Cells: The Architects of
1228 Skeletal Muscle." *Current Topics in Developmental Biology* 107:161–81.
1229 Chen, Ieng-Yi, Jacqueline Lypowy, Jayashree Pain, Danish Sayed, Stan Grinberg, Ralph R.

1230 Alcendor, Junichi Sadoshima, and Maha Abdellatif. 2006. “Histone H2A.z Is Essential
1231 for Cardiac Myocyte Hypertrophy but Opposed by Silent Information Regulator 2α*.”
1232 *The Journal of Biological Chemistry* 281 (28): 19369–77.
1233 Chen, Poshen B., Hsiuyi V. Chen, Diwash Acharya, Oliver J. Rando, and Thomas G. Fazzio.
1234 2015. “R Loops Regulate Promoter-Proximal Chromatin Architecture and Cellular
1235 Differentiation.” *Nature Structural & Molecular Biology* 22 (12): 999–1007.
1236 Chereau, David, Malgorzata Boczkowska, Aneta Skwarek-Maruszewska, Ikuko Fujiwara,
1237 David B. Hayes, Grzegorz Rebowski, Pekka Lappalainen, Thomas D. Pollard, and
1238 Roberto Dominguez. 2008. “Leiomodin Is an Actin Filament Nucleator in Muscle Cells.”
1239 *Science* 320 (5873): 239–43.
1240 Codato, Roberta, Martine Perichon, Arnaud Divol, Ella Fung, Athanassia Sotiropoulos, Anne
1241 Bigot, Jonathan B. Weitzman, and Souhila Medjkane. 2019. “The SMYD3
1242 Methyltransferase Promotes Myogenesis by Activating the Myogenin Regulatory
1243 Network.” *Scientific Reports* 9 (1): 1–14.
1244 Conley, C. A. 2001. “Leiomodin and Tropomodulin in Smooth Muscle.” *American Journal of*
1245 *Physiology. Cell Physiology* 280 (6): C1645–56.
1246 Conley, C. A., K. L. Fritz-Six, A. Almenar-Queralt, and V. M. Fowler. 2001. “Leiomodins:
1247 Larger Members of the Tropomodulin (Tmod) Gene Family.” *Genomics* 73 (2): 127–39.
1248 Cui, Can, Shunshun Han, Xiaoxu Shen, Haorong He, Yuqi Chen, Jing Zhao, Yuanhang Wei,
1249 et al. 2020. “ISLR Regulates Skeletal Muscle Atrophy via IGF1-PI3K/Akt-Foxo Signaling
1250 Pathway.” *Cell and Tissue Research* 381 (3): 479–92.
1251 Diaz-Ruiz, Alberto, Marta Gonzalez-Freire, Luigi Ferrucci, Michel Bernier, and Rafael de
1252 Cabo. 2015. “SIRT1 Synchs Satellite Cell Metabolism with Stem Cell Fate.” *Cell Stem*
1253 *Cell* 16 (2): 103–4.
1254 Dos Santos, Matthieu, Akansha M. Shah, Yichi Zhang, Svetlana Bezprozvannaya, Kenian
1255 Chen, Lin Xu, Weichun Lin, et al. 2023. “Opposing Gene Regulatory Programs
1256 Governing Myofiber Development and Maturation Revealed at Single Nucleus
1257 Resolution.” *Nature Communications* 14 (1): 1–14.
1258 Eliazer, Susan, Jonathon M. Muncie, Josef Christensen, Xuefeng Sun, Rebecca S. D’Urso,
1259 Valerie M. Weaver, and Andrew S. Brack. 2019. “Wnt4 from the Niche Controls the
1260 Mechano-Properties and Quiescent State of Muscle Stem Cells.” *Cell Stem Cell* 25 (5):
1261 654–65.e4.
1262 Finke, Daniel, Leonard M. Schanze, Friederike Schreiter, Michael M. Kreußer, Hugo A.
1263 Katus, Johannes Backs, and Lorenz H. Lehmann. 2022. “Histone Deacetylase 4
1264 Deletion Broadly Affects Cardiac Epigenetic Repression and Regulates Transcriptional
1265 Susceptibility via H3K9 Methylation.” *Journal of Molecular and Cellular Cardiology* 162
1266 (January):119–29.
1267 Fowler, Velia M., and Roberto Dominguez. 2017. “Tropomodulins and Leiomodins: Actin
1268 Pointed End Caps and Nucleators in Muscles.” *Biophysical Journal* 112 (9): 1742–60.
1269 Fre, Silvia, Mathilde Huyghe, Philippos Mourikis, Sylvie Robine, Daniel Louvard, and Spyros
1270 Artavanis-Tsakonas. 2005. “Notch Signals Control the Fate of Immature Progenitor
1271 Cells in the Intestine.” *Nature* 435 (7044): 964–68.
1272 Friedrichs, Melanie, Florian Wirsdöerfer, Stefanie B. Flohé, Sabine Schneider, Manuela
1273 Wuelling, and Andrea Vortkamp. 2011. “BMP Signaling Balances Proliferation and
1274 Differentiation of Muscle Satellite Cell Descendants.” *BMC Cell Biology* 12 (June):26.
1275 Fulco, Marcella, Yana Cen, Po Zhao, Eric P. Hoffman, Michael W. McBurney, Anthony A.
1276 Sauve, and Vittorio Sartorelli. 2008. “Glucose Restriction Inhibits Skeletal Myoblast
1277 Differentiation by Activating SIRT1 through AMPK-Mediated Regulation of Nampt.”

Developmental Cell 14 (5): 661–73.
Fulco, Marcella, R. Louis Schiltz, Simona Iezzi, M. Todd King, Po Zhao, Yoshihiro Kashiwaya, Eric Hoffman, Richard L. Veech, and Vittorio Sartorelli. 2003. “Sir2 Regulates Skeletal Muscle Differentiation as a Potential Sensor of the Redox State.” *Molecular Cell* 12 (1): 51–62.
Fu, Xin, Huating Wang, and Ping Hu. 2015. “Stem Cell Activation in Skeletal Muscle Regeneration.” *Cellular and Molecular Life Sciences: CMLS* 72 (9): 1663–77.
Ganassi, Massimo, Sara Badodi, Kees Wanders, Peter S. Zammit, and Simon M. Hughes. 2020. “Myogenin Is an Essential Regulator of Adult Myofibre Growth and Muscle Stem Cell Homeostasis.” *eLife* 9 (October). https://doi.org/10.7554/eLife.60445.
Gorynia, Sabine, Tiago M. Bandeiras, Filipa G. Pinho, Colin E. McVey, Clemens Vonrhein, Adam Round, Dmitri I. Svergun, Peter Donner, Pedro M. Matias, and Maria Arménia Carrondo. 2011. “Structural and Functional Insights into a Dodecameric Molecular Machine - the RuvBL1/RuvBL2 Complex.” *Journal of Structural Biology* 176 (3): 279–91.
Grifone, Raphaëlle, Audrey Saquet, Manon Desgres, Claudia Sangiorgi, Caterina Gargano, Zhenlin Li, Dario Coletti, and De-Li Shi. 2021. “Rbm24 Displays Dynamic Functions Required for Myogenic Differentiation during Muscle Regeneration.” *Scientific Reports* 11 (1): 9423.
Guerin, Colleen M., and Sunita G. Kramer. 2009. “Cytoskeletal Remodeling during Myotube Assembly and Guidance: Coordinating the Actin and Microtubule Networks.” *Communicative & Integrative Biology* 2 (5): 452–57.
Heng, Yi-Wen, and Cheng-Gee Koh. 2010. “Actin Cytoskeleton Dynamics and the Cell Division Cycle.” *The International Journal of Biochemistry & Cell Biology* 42 (10): 1622–33.
Higuchi-Sanabria, Ryo, Joseph W. Paul, Jenni Durieux, Camila Benitez, Phillip A. Frankino, Sarah U. Tronnes, Gilberto Garcia, Joseph R. Daniele, Samira Monshietehadi, and Andrew Dillin. 2018. “Spatial Regulation of the Actin Cytoskeleton by HSF-1 during Aging.” *Molecular Biology of the Cell* 29 (21): 2522–27.
Hindi, Lubna, Joseph D. McMillan, Dil Afroze, Sajedah M. Hindi, and Ashok Kumar. 2017. “Isolation, Culturing, and Differentiation of Primary Myoblasts from Skeletal Muscle of Adult Mice.” *Bio-Protocol* 7 (9). https://doi.org/10.21769/BioProtoc.2248.
Hisahara, Shin, Susumu Chiba, Hiroyuki Matsumoto, Masaya Tanno, Hideshi Yagi, Shun Shimohama, Makoto Sato, and Yoshiyuki Horio. 2008. “Histone Deacetylase SIRT1 Modulates Neuronal Differentiation by Its Nuclear Translocation.” *Proceedings of the National Academy of Sciences of the United States of America* 105 (40): 15599–604.
Horio, Yoshiyuki, Takashi Hayashi, Atsushi Kuno, and Risa Kunimoto. 2011. “Cellular and Molecular Effects of Sirtuins in Health and Disease.” *Clinical Science* 121 (5): 191–203.
Hung, Margaret, Hsiao-Fan Lo, Grace E. L. Jones, and Robert S. Krauss. 2023. “The Muscle Stem Cell Niche at a Glance.” *Journal of Cell Science* 136 (24). https://doi.org/10.1242/jcs.261200.
Hunt, Liam C., Aradhana Upadhyay, Jalal A. Jazayeri, Elizabeth M. Tudor, and Jason D. White. 2013. “An Anti-Inflammatory Role for Leukemia Inhibitory Factor Receptor Signaling in Regenerating Skeletal Muscle.” *Histochemistry and Cell Biology* 139 (1): 13–34.
Hwang, Ara B., and Andrew S. Brack. 2018. “Muscle Stem Cells and Aging.” *Current Topics in Developmental Biology* 126:299–322.
Kim, Kun Ho, Jiamin Qiu, and Shihuan Kuang. 2020. “Isolation, Culture, and Differentiation of Primary Myoblasts Derived from Muscle Satellite Cells.” *Bio-Protocol* 10 (14): e3686.

1326 Kim, Yu Jin, Min Jeong Cho, Won Dong Yu, Myung Joo Kim, Sally Yunsun Kim, and Jae Ho
1327 Lee. 2022. “Links of Cytoskeletal Integrity with Disease and Aging.” *Cells* 11 (18).
1328 https://doi.org/10.3390/cells11182896.
1329 Kislinger, Thomas, Anthony O. Gramolini, Yan Pan, Khaled Rahman, David H. MacLennan,
1330 and Andrew Emili. 2005. “Proteome Dynamics during C2C12 Myoblast Differentiation.”
1331 *Molecular & Cellular Proteomics: MCP* 4 (7): 887–901.
1332 Knight, James Dr, and Rashmi Kothary. 2011. “The Myogenic Kinome: Protein Kinases
1333 Critical to Mammalian Skeletal Myogenesis.” *Skeletal Muscle* 1 (September):29.
1334 Lai, Wing-Fu, and Wing-Tak Wong. 2020. “Roles of the Actin Cytoskeleton in Aging and
1335 Age-Associated Diseases.” *Ageing Research Reviews* 58 (March):101021.
1336 Lakisic, Goran, Alice Lebreton, Renaud Pourpre, Olivia Wendling, Emanuele Libertini,
1337 Elizabeth J. Radford, Morwenna Le Guillou, et al. 2016. “Role of the BAHD1 Chromatin-
1338 Repressive Complex in Placental Development and Regulation of Steroid Metabolism.”
1339 *PLoS Genetics* 12 (3): e1005898.
1340 Larraín, J., J. Alvarez, J. R. Hassell, and E. Brandan. 1997. “Expression of Perlecan, a
1341 Proteoglycan That Binds Myogenic Inhibitory Basic Fibroblast Growth Factor, Is down
1342 Regulated during Skeletal Muscle Differentiation.” *Experimental Cell Research* 234 (2):
1343 405–12.
1344 Larsson, Lars, Hans Degens, Meishan Li, Leonardo Salviati, Young Il Lee, Wesley
1345 Thompson, James L. Kirkland, and Marco Sandri. 2019. “Sarcopenia: Aging-Related
1346 Loss of Muscle Mass and Function.” *Physiological Reviews* 99 (1): 427–511.
1347 Lepper, Christoph, Terence A. Partridge, and Chen-Ming Fan. 2011. “An Absolute
1348 Requirement for Pax7-Positive Satellite Cells in Acute Injury-Induced Skeletal Muscle
1349 Regeneration.” *Development* 138 (17): 3639–46.
1350 Liao, Yuxing, Jing Wang, Eric J. Jaehnig, Zhiao Shi, and Bing Zhang. 2019. “WebGestalt
1351 2019: Gene Set Analysis Toolkit with Revamped UIs and APIs.” *Nucleic Acids Research*
1352 47 (W1): W199–205.
1353 Lukjanenko, Laura, M. Juliane Jung, Nagabhooshan Hegde, Claire Perruisseau-Carrier,
1354 Eugenia Migliavacca, Michelle Rozo, Sonia Karaz, et al. 2016. “Loss of Fibronectin from
1355 the Aged Stem Cell Niche Affects the Regenerative Capacity of Skeletal Muscle in
1356 Mice.” *Nature Medicine* 22 (8): 897–905.
1357 Lu-Nguyen, Ngoc, Alberto Malerba, Linda Popplewell, Fred Schnell, Gunnar Hanson, and
1358 George Dickson. 2017. “Systemic Antisense Therapeutics for Dystrophin and Myostatin
1359 Exon Splice Modulation Improve Muscle Pathology of Adult Mdx Mice.” *Molecular*
1360 *Therapy. Nucleic Acids* 6 (March):15–28.
1361 Mackmull, Marie-Therese, Bernd Klaus, Ivonne Heinze, Manopriya Chokkalingam, Andreas
1362 Beyer, Robert B. Russell, Alessandro Ori, and Martin Beck. 2017. “Landscape of
1363 Nuclear Transport Receptor Cargo Specificity.” *Molecular Systems Biology* 13 (12): 962.
1364 Maltzahn, Julia von, Andrew E. Jones, Robin J. Parks, and Michael A. Rudnicki. 2013. “Pax7
1365 Is Critical for the Normal Function of Satellite Cells in Adult Skeletal Muscle.”
1366 *Proceedings of the National Academy of Sciences of the United States of America* 110
1367 (41): 16474–79.
1368 Massenet, Jimmy, Edward Gardner, Bénédicte Chazaud, and F. Jeffrey Dilworth. 2021.
1369 “Epigenetic Regulation of Satellite Cell Fate during Skeletal Muscle Regeneration.”
1370 *Skeletal Muscle* 11 (1): 4.
1371 Mauro, A. 1961. “Satellite Cell of Skeletal Muscle Fibers.” *The Journal of Biophysical and*
1372 *Biochemical Cytology* 9 (2): 493–95.
1373 Meyer, Gretchen A., Simon Schenk, and Richard L. Lieber. 2013. “Role of the Cytoskeleton

in Muscle Transcriptional Responses to Altered Use." *Physiological Genomics* 45 (8): 321–31.

Moresi, Viviana, Michele Carrer, Chad E. Grueter, Oktay F. Rifki, John M. Shelton, James A. Richardson, Rhonda Bassel-Duby, and Eric N. Olson. 2012. "Histone Deacetylases 1 and 2 Regulate Autophagy Flux and Skeletal Muscle Homeostasis in Mice." *Proceedings of the National Academy of Sciences of the United States of America* 109 (5): 1649–54.

Mournetas, Virginie, Emmanuelle Massouridès, Jean-Baptiste Dupont, Etienne Kornobis, Hélène Polvèche, Margot Jarrige, Alan R. L. Dorval, et al. 2021. "Myogenesis Modelled by Human Pluripotent Stem Cells: A Multi-Omic Study of Duchenne Myopathy Early Onset." *Journal of Cachexia, Sarcopenia and Muscle* 12 (1): 209–32.

Moynihan, Kathryn A., Andrew A. Grimm, Marie M. Plueger, Ernesto Bernal-Mizrachi, Eric Ford, Corentin Cras-Méneur, M. Alan Permutt, and Shin-Ichiro Imai. 2005. "Increased Dosage of Mammalian Sir2 in Pancreatic Beta Cells Enhances Glucose-Stimulated Insulin Secretion in Mice." *Cell Metabolism* 2 (2): 105–17.

Murphy, Malea M., Jennifer A. Lawson, Sam J. Mathew, David A. Hutcheson, and Gabrielle Kardon. 2011. "Satellite Cells, Connective Tissue Fibroblasts and Their Interactions Are Crucial for Muscle Regeneration." *Development* 138 (17): 3625–37.

Nanda, Vivek, and Joseph M. Miano. 2012. "Leiomodin 1, a New Serum Response Factor-Dependent Target Gene Expressed Preferentially in Differentiated Smooth Muscle Cells." *The Journal of Biological Chemistry* 287 (4): 2459–67.

Nanda, Vivek, Ting Wang, Milos Pjanic, Boxiang Liu, Trieu Nguyen, Ljubica Perisic Matic, Ulf Hedin, et al. 2018. "Functional Regulatory Mechanism of Smooth Muscle Cell-Restricted LMOD1 Coronary Artery Disease Locus." *PLoS Genetics* 14 (11): e1007755.

Nauen, David W., Michael C. Haffner, Juyun Kim, Qizhi Zheng, Hao Yin, Angelo M. DeMarzo, Vasiliki Mahairaki, Carlo Colantuoni, J. Geoffrey Pickering, and Tory P. Johnson. 2020. "Putative Autoantigen Leiomodin-1 Is Expressed in the Human Brain and in the Membrane Fraction of Newly Formed Neurons." *Pathogens* 9 (12). https://doi.org/10.3390/pathogens9121036.

Nguyen, Mai Thi, You Han Won, Tae Won Kwon, and Wan Lee. 2022. "Twinfilin-1 Is an Essential Regulator of Myogenic Differentiation through the Modulation of YAP in C2C12 Myoblasts." *Biochemical and Biophysical Research Communications* 599 (April):17–23.

Peck, Barrie, Chun-Yuan Chen, Ka-Kei Ho, Paolo Di Fruscia, Stephen S. Myatt, R. Charles Coombes, Matthew J. Fuchter, Chwan-Deng Hsiao, and Eric W-F Lam. 2010. "SIRT Inhibitors Induce Cell Death and p53 Acetylation through Targeting Both SIRT1 and SIRT2." *Molecular Cancer Therapeutics* 9 (4): 844–55.

Pfaffl, M. W. 2001. "A New Mathematical Model for Relative Quantification in Real-Time RT-PCR." *Nucleic Acids Research* 29 (9): e45.

Pollard, Thomas D., and John A. Cooper. 2009. "Actin, a Central Player in Cell Shape and Movement." *Science* 326 (5957): 1208–12.

Qualmann, Britta, and Michael M. Kessels. 2009. "New Players in Actin Polymerization--WH2-Domain-Containing Actin Nucleators." *Trends in Cell Biology* 19 (6): 276–85.

Ryall, James G., Stefania Dell'Orso, Assia Derfoul, Aster Juan, Hossein Zare, Xuesong Feng, Daphney Clermont, et al. 2015. "The NAD(+)-Dependent SIRT1 Deacetylase Translates a Metabolic Switch into Regulatory Epigenetics in Skeletal Muscle Stem Cells." *Cell Stem Cell* 16 (2): 171–83.

Saccone, Valentina, and Pier Lorenzo Puri. 2010. "Epigenetic Regulation of Skeletal

Myogenesis." *Organogenesis* 6 (1): 48–53.
Sambasivan, Ramkumar, Roseline Yao, Adrien Kissenpfennig, Laetitia Van Wittenberghe, Andràs Paldi, Barbara Gayraud-Morel, Hind Guenou, Bernard Malissen, Shahragim Tajbakhsh, and Anne Galy. 2011. "Pax7-Expressing Satellite Cells Are Indispensable for Adult Skeletal Muscle Regeneration." *Development* 138 (17): 3647–56.
Schmidt, Manuel, Svenja C. Schüler, Sören S. Hüttner, Björn von Eyss, and Julia von Maltzahn. 2019. "Adult Stem Cells at Work: Regenerating Skeletal Muscle." *Cellular and Molecular Life Sciences: CMLS* 76 (13): 2559–70.
Schüler, Svenja C., Joanna M. Kirkpatrick, Manuel Schmidt, Deolinda Santinha, Philipp Koch, Simone Di Sanzo, Emilio Cirri, Martin Hemberg, Alessandro Ori, and Julia von Maltzahn. 2021. "Extensive Remodeling of the Extracellular Matrix during Aging Contributes to Age-Dependent Impairments of Muscle Stem Cell Functionality." *Cell Reports* 35 (10): 109223.
Seale, Patrick. 2003. *Pax7 Is Required for Muscle Satellite Cell Specification and Regenerative Myogenesis*. McMaster University.
Shefer, Gabi, Daniel P. Van de Mark, Joshua B. Richardson, and Zipora Yablonka-Reuveni. 2006. "Satellite-Cell Pool Size Does Matter: Defining the Myogenic Potency of Aging Skeletal Muscle." *Developmental Biology* 294 (1): 50–66.
Sousa-Victor, Pedro, Laura García-Prat, Antonio L. Serrano, Eusebio Perdiguero, and Pura Muñoz-Cánoves. 2015. "Muscle Stem Cell Aging: Regulation and Rejuvenation." *Trends in Endocrinology and Metabolism: TEM* 26 (6): 287–96.
Sousa-Victor, Pedro, Susana Gutarra, Laura García-Prat, Javier Rodriguez-Ubreva, Laura Ortet, Vanessa Ruiz-Bonilla, Mercè Jardí, et al. 2014. "Geriatric Muscle Stem Cells Switch Reversible Quiescence into Senescence." *Nature* 506 (7488): 316–21.
Szklarczyk, Damian, Andrea Franceschini, Michael Kuhn, Milan Simonovic, Alexander Roth, Pablo Minguez, Tobias Doerks, et al. 2011. "The STRING Database in 2011: Functional Interaction Networks of Proteins, Globally Integrated and Scored." *Nucleic Acids Research* 39 (Database issue): D561–68.
Tanno, Masaya, Atsushi Kuno, Toshiyuki Yano, Tetsuji Miura, Shin Hisahara, Satoko Ishikawa, Kazuaki Shimamoto, and Yoshiyuki Horio. 2010. "Induction of Manganese Superoxide Dismutase by Nuclear Translocation and Activation of SIRT1 Promotes Cell Survival in Chronic Heart Failure." *The Journal of Biological Chemistry* 285 (11): 8375–82.
Tanno, Masaya, Jun Sakamoto, Tetsuji Miura, Kazuaki Shimamoto, and Yoshiyuki Horio. 2007. "Nucleocytoplasmic Shuttling of the NAD+-Dependent Histone Deacetylase SIRT1." *The Journal of Biological Chemistry* 282 (9): 6823–32.
Tannu, Nilesh S., Vamshi K. Rao, Ritcha M. Chaudhary, Francesco Giorgianni, Abdelwahab E. Saeed, Yong Gao, and Rajendra Raghow. 2004. "Comparative Proteomes of the Proliferating C2C12 Myoblasts and Fully Differentiated Myotubes Reveal the Complexity of the Skeletal Muscle Differentiation Program." *Molecular & Cellular Proteomics: MCP* 3 (11): 1065–82.
Tiffin, N., R. D. Williams, J. Shipley, and K. Pritchard-Jones. 2003. "PAX7 Expression in Embryonal Rhabdomyosarcoma Suggests an Origin in Muscle Satellite Cells." *British Journal of Cancer* 89 (2): 327–32.
Tolkatchev, Dmitri, Carol C. Gregorio, and Alla S. Kostyukova. 2022. "The Role of Leiomodin in Actin Dynamics: A New Road or a Secret Gate." *The FEBS Journal* 289 (20): 6119–31.
Tong, Chao, Alex Morrison, Samantha Mattison, Su Qian, Mark Bryniarski, Bethany Rankin,

1470 Jun Wang, D. Paul Thomas, and Ji Li. 2013. “Impaired SIRT1 Nucleocytoplasmic
1471 Shuttling in the Senescent Heart during Ischemic Stress.” *FASEB Journal: Official*
1472 *Publication of the Federation of American Societies for Experimental Biology* 27 (11):
1473 4332–42.
1474 Tsukada, Takehiro, Christopher T. Pappas, Natalia Moroz, Parker B. Antin, Alla S.
1475 Kostyukova, and Carol C. Gregorio. 2010. “Leiomodin-2 Is an Antagonist of
1476 Tropomodulin-1 at the Pointed End of the Thin Filaments in Cardiac Muscle.” *Journal of*
1477 *Cell Science* 123 (Pt 18): 3136–45.
1478 Vachharajani, Vidula T., Tiefu Liu, Xianfeng Wang, Jason J. Hoth, Barbara K. Yoza, and
1479 Charles E. McCall. 2016. “Sirtuins Link Inflammation and Metabolism.” *Journal of*
1480 *Immunology Research* 2016 (January):8167273.
1481 Voronova, Anastassia, Erin Coyne, Ashraf Al Madhoun, Joel V. Fair, Neven Bosiljcic,
1482 Catherine St-Louis, Grace Li, et al. 2013. “Hedgehog Signaling Regulates MyoD
1483 Expression and Activity.” *The Journal of Biological Chemistry* 288 (6): 4389–4404.
1484 Wang, Dongdong, Dandan Zhao, Yuan Li, Tingjun Dai, Fuchen Liu, and Chuanzhu Yan.
1485 2022. “TGM2 Positively Regulates Myoblast Differentiation via Enhancing the mTOR
1486 Signaling.” *Biochimica et Biophysica Acta, Molecular Cell Research* 1869 (3): 119173.
1487 Winder, S. J., T. J. Gibson, and J. Kendrick-Jones. 1995. “Dystrophin and Utrophin: The
1488 Missing Links!” *FEBS Letters* 369 (1): 27–33.
1489 Winter, Lilli, and Gerhard Wiche. 2013. “The Many Faces of Plectin and Plectinopathies:
1490 Pathology and Mechanisms.” *Acta Neuropathologica* 125 (1): 77–93.
1491 Xie, Xin, S. Raza Mahmood, Tamara Gjorgjieva, and Piergiorgio Percipalle. 2020. “Emerging
1492 Roles of Cytoskeletal Proteins in Regulating Gene Expression and Genome
1493 Organization during Differentiation.” *Nucleus* 11 (1): 53–65.
1494 Yamakawa, Hiroyuki, Dai Kusumoto, Hisayuki Hashimoto, and Shinsuke Yuasa. 2020.
1495 “Stem Cell Aging in Skeletal Muscle Regeneration and Disease.” *International Journal of*
1496 *Molecular Sciences* 21 (5). https://doi.org/10.3390/ijms21051830.
1497 Yamane, A., K. Takahashi, M. Mayo, H. Vo, L. Shum, M. Zeichner-David, and H. C. Slavkin.
1498 1998. “Induced Expression of myoD, Myogenin and Desmin during Myoblast
1499 Differentiation in Embryonic Mouse Tongue Development.” *Archives of Oral Biology* 43
1500 (5): 407–16.
1501 Yang, Pengyi, Xiaofeng Zheng, Vivek Jayaswal, Guang Hu, Jean Yee Hwa Yang, and Raja
1502 Jothi. 2015. “Knowledge-Based Analysis for Detecting Key Signaling Events from Time-
1503 Series Phosphoproteomics Data.” *PLoS Computational Biology* 11 (8): e1004403.
1504 Yuen, Michaela, Lisa Worgan, Jessika Iwanski, Christopher T. Pappas, Himanshu Joshi,
1505 Jared M. Churko, Susan Arbuckle, et al. 2022. “Neonatal-Lethal Dilated
1506 Cardiomyopathy due to a Homozygous LMOD2 Donor Splice-Site Variant.” *European*
1507 *Journal of Human Genetics: EJHG* 30 (4): 450–57.
1508 Zammit, Peter S., Frederic Relaix, Yosuke Nagata, Ana Pérez Ruiz, Charlotte A. Collins,
1509 Terence A. Partridge, and Jonathan R. Beauchamp. 2006. “Pax7 and Myogenic
1510 Progression in Skeletal Muscle Satellite Cells.” *Journal of Cell Science* 119 (Pt 9):
1511 1824–32.
1512 Zhang, Kuo, Yuying Zhang, Lijie Gu, Miaomiao Lan, Chuncheng Liu, Meng Wang, Yang Su,
1513 et al. 2018. “Islr Regulates Canonical Wnt Signaling-Mediated Skeletal Muscle
1514 Regeneration by Stabilizing Dishevelled-2 and Preventing Autophagy.” *Nature*
1515 *Communications* 9 (1): 1–16.